Citation
Huang, Z. and Chen, W. and Hao, H. and Chen, Z. and Pham, T.M. and Tran, T.T. and Elchalakani, M. 2021. Flexural behaviour of ambient cured geopolymer concrete beams reinforced with BFRP bars under static and impact loads. Composite Structures. 261: ARTN 113282. http://doi.org/10.1016/j.compstruct.2020.113282

Flexural Behaviour of Ambient Cured Geopolymer Concrete Beams Reinforced with BFRP Bars under Static and Impact Loads

Zhijie Huang[1,2], Wensu Chen[1*], Hong Hao[1*], Zuyu Chen[2], Thong M. Pham[1], Tung T. Tran[1], Mohamed Elchalakani[3]

1. Center for Infrastructural Monitoring and Protection, School of Civil and Mechanical Engineering, Curtin University, Australia

2. Institute of Geotechnical Engineering, Zhejiang University, Hangzhou 310058, China

3. School of Civil, Environmental and Mining Engineering, The University of Western Australia, 35 Stirling Highway, WA 6009, Australia

*Corresponding authors. E-mail addresses: wensu.chen@curtin.edu.au (W. Chen), hong.hao@curtin.edu.au (H. Hao).

Abstract: The applications of GeoPolymer Concrete (GPC) with basalt-fiber-reinforced-polymer (BFRP) reinforcements could be alternative for conventional structural designs with Portland Cement Concrete reinforced with steel bars for green and sustainable constructions. Very limited studies, however, have been carried out to investigate the performance of GPC beams reinforced with BFRP bars subjected to static loads, and no study of their performance under impact load is available in open literature yet. In this study, ambient-cured GPC beams reinforced with BFRP bars were tested under static and impact loads. Their damage modes, static and dynamic responses were recorded and analysed. The test results showed that the beams experienced flexural failure mode under static load while combined flexure-shear failure mode was observed under impact load. The impact-loading tested beams were further statically loaded to examine their residual capacities. Additionally, numerical models of the tested GPC beams were developed adopting the commonly used concrete material model *Mat_072R3 (KCC model) in LS-DYNA with modified parameters based on the GPC material test data. The calibrated numerical model was used for parametric simulations. The results showed that with the increased impact velocity, failure mode of the beam shifted from the flexure-governed to punching-shear-governed along with the rupture of longitudinal BFRP bars.

Keywords: GeoPolymer Concrete beam; BFRP bar; Static test; Impact test; Numerical simulation

1. Introduction

Climate change due to the greenhouse gas emission is one of the most important issues. Ordinary Portland Cement Concrete (OPC) is the most widely used construction material around the world. Producing OPC results in large amounts of carbon dioxide (CO_2) emission. It is estimated that the production of cement contributes to 5-7% of global CO_2 emission [1-4] because the manufacturing of cement is energy intensive since the raw materials need to be heated at the temperatures up to 1350 ^oC [5]. Therefore, replacing OPC with GeoPolymer Concrete (GPC) in construction is a promising solution to reduce CO_2 emission. GPC is formed by an alkali-activated polymeric reaction of alumina-silicate source materials binding aggregates and other un-reacted materials [6]. The source materials such as fly ash and slag are industrial wastes. Reuse of these industry waste materials in construction also leads to enormous benefits to environment, saves large land areas for waste disposals. GPC also has many other attractive properties such as good fire resistance, good resistance to acid attack, and can be mixed to reach desirable strengths, etc. [7, 8]. The material properties of GPC have been studied [9-16] and some GPC structural elements have already been used in construction [17].

On the other hand, corrosion of steel reinforcement in conventional construction imposes a significant sustainability problem to the built structures. Corrosion damage of steel reinforcements reduces structural strength, and could lead to catastrophic structural collapse in extreme situations. Therefore it requires careful monitoring of the structural conditions and retrofitting the corrosion damaged structures, which greatly increases the lifecycle maintenance cost of steel reinforced structures, especially those in coastal areas. As compared to the conventional steel reinforcements in concrete structures, fiber-reinforced-polymer (FRP) reinforcements have the advantages of high tensile strength, lightweight, good corrosion resistance, and fatigue endurance [18], which make them a practical alternative to conventional steel reinforcements.

Over the past decades, many efforts have been made to investigate the performance of OPC beams reinforced with FRP bars under static load [19-27]. The existing standards for FRP bars used in OPC structures include CSA S806 [28] and ACI 440.1R [29]. However, very limited studies were carried out to explore the behaviour of GPC beams reinforced with FRP bars under static load. Maranan et al. [30] conducted four-point bending tests to investigate the effects of reinforcement diameter, reinforcement ratio, and anchorage system on the flexural strength and serviceability of GPC beams reinforced with glass-fiber-reinforced-polymer (GFRP) bars. The test results showed that given the similar reinforcement ratio, the diameter of the GFRP bars had no significant effect on the flexural performance of the tested beams. The serviceability performance of the beams would be enhanced with the increasing reinforcement ratio. Fan and Zhang [31] compared the performances of inorganic polymer concrete (IPC, also called GPC) beams reinforced with basalt-fiber-reinforced-polymer (BFRP) bars with those of OPC beams reinforced with steel bars. The test results showed that the IPC beams exhibited a two-stage load-midspan deflection curve, namely an uncracked stage and a post-cracking stage before complete failure. No clear yielding region was observed due to the linear elastic properties of BFRP bars as compared with the steel reinforced IPC beams. The crack patterns of these two types of beams were similar while the BFRP reinforced IPC beams had a much larger maximum crack width due to the lower elastic modulus of BFRP bars as compared to steel bars. However, the test results by other researchers on both OPC and GPC beams reinforced with FRP bars experienced three-stage load-midspan deflection curves, i.e., an uncracked stage, a post-cracking stage, and a post-concrete crushing stage that the beam could carry further load after concrete started crushing [30, 32-34]. Maranan et al. [30] considered this behaviour could be due to the confinement effect provided by the FRP stirrups that enhanced the ductility and strength of the beams. Ahmed et al. [35] investigated the influence of reinforcement ratio, GPC compressive strength, and concrete types on the flexural behaviour of GPC beams reinforced with carbon-fiber-reinforced-polymer (CFRP) bars. The test results showed that the concrete compressive strength had a significant effect on the cracking load. It was found that the predicted results based on CSA S806-12 [28] and ACI 440.1R-15 [29] underestimated the flexural strength of the tested beams.

Concrete structures may be subjected to impact loads, such as rock fall, vehicle impact, and terrorist attacks during their service life. Previous studies mainly focused on the impact behaviour of OPC beams reinforced with conventional steel reinforcements [36-39] and very limited studies on the impact behaviour of OPC beams reinforced with FRP bars [32, 33, 40, 41] were reported in recent years. Goldston et al. [32, 33] studied the performances of normal strength concrete (NSC), high strength concrete (HSC), and ultra-high strength concrete (UHSC) beams reinforced with GFRP bars under static and impact loads. The effects of reinforcement ratio, concrete strength, and dropping height were investigated and an average dynamic amplification factor (DAF) of 1.15-1.17 of the experimental dynamic moment capacity was obtained with respect to the static moment capacity. Numerical models were also built to investigate the influence of reinforcement ratio, concrete strength, drop weight, drop velocity, and impact energy on the responses of OPC beams reinforced with GFRP bars [40]. Saleh et al. [41] explored the shear behaviour of OPC beams reinforced with GFRP bars by varying the stirrup spacing and dropping height. It was found that the beams with higher shear capacities failed in flexure and flexure-shear, whereas those with lower shear capacities failed in shear-plug manner.

No study can be found in open literature on the dynamic behaviour of GPC beams reinforced with FRP bars under impact load. Since the inherent material properties of GPC are different from those of OPC, e.g., GPC is more brittle than OPC and behaves differently in post failure stage [42], the impact responses of GPC beams reinforced with FRP bars could be different from those of OPC beams. In this study, three ambient-cured GPC beams reinforced with BFRP bars were prepared. One beam was tested under static load as a reference beam while the other two beams were tested under impact load to ensure the repeatability. The responses of the beams under static and impact loads were compared and analysed in terms of failure mode, crack pattern, and load-deflection relation. In addition, numerical model was built and calibrated against the experimental results. The effect of impact velocities on the failure mode of the beams was also investigated through numerical simulations.

2. Experimental program

2.1. Material

2.1.1 Geopolymer concrete

The ambient-cured GPC used in the study consisted of fly ash, slag, alkaline solution, sand and coarse aggregates. The alkaline solution used was a mixture of 12 M sodium hydroxide (NaOH) and commercial D-grade sodium silicate (Na_2SiO_3) solution. Coarse aggregates had the average sizes of 7 mm and 10 mm with the proportions of 50% and 50%, respectively. The mix design was developed based on the previous studies [12, 16, 43] and given in **Table 1** to achieve compressive strength of 40 MPa.

Table 1 Mix proportion of GPC (kg/m^3)

Coarse aggregates	Sand	Binder		Solution		Alkaline solution/binder ratio
		Fly ash	Slag	Na_2SiO_3	NaOH	
1196	644	360	40	173.7	59.4	0.6

2.1.2 BFRP bar

The BFRP bars used in this study consisted of basalt fibers as a reinforcing material and epoxy resin as a matrix material. The beam reinforcement cages were made of longitudinal BFRP bars and BFRP stirrups with 10 mm nominal diameter as shown in **Fig. 1**. The ultimate tensile strength f_{fu}, elastic modulus E_f, and elongation ε_{fu} of BFRP bars provided by supplier [44] were 1200 MPa, 55 GPa, and 0.02, respectively.

Fig. 1. BFRP cage for beam casting

2.2. Beam specimens

The beams were designed to have the dimensions of width (b) 150 mm, height (h) 200 mm, and total length (L_t) 1250 mm. **Fig. 2** shows the beam section and the reinforcements. The beams were longitudinally reinforced with four 10 mm-diameter BFRP bars and transversely reinforced with 10 mm-diameter BFRP stirrups at 100 mm spacing as shown in **Fig. 1**. Only one beam was tested under static load (three-point bending) while another two beams were examined under impact load (drop hammer impact) to ensure the repeatability. To investigate the flexural behaviour of BFRP bars reinforced GPC beams, the beams were designed with their flexural capacities (i.e. 64 kN) about half of the shear capacities (i.e. 132 kN). Since there is no standard available for the design of GPC beams reinforced with FRP bars, the code ACI 440.1R-15 [29] for OPC beams was adopted for the design in this study. The tensile reinforcement ratio ρ_f was 0.63%, much higher than the balanced reinforcement ratio ρ_{fb} (about 0.26%), indicating that all the beams were over-reinforced and the failure was controlled by the concrete crushing under static load. **Table 2** summarizes the details of the tested beams. For easy reference, the beam labels include three parts: the first part is the concrete type, i.e., GPC; the second part with the letters of "S" and "I" represents the loading conditions, namely static load and impact load, respectively; the last number denotes the concrete compressive strength f_c'. For example, Beam GPC-I-44 means the beam with the concrete strength of 44 MPa was tested under impact load. All the beams were cast and cured under ambient condition.

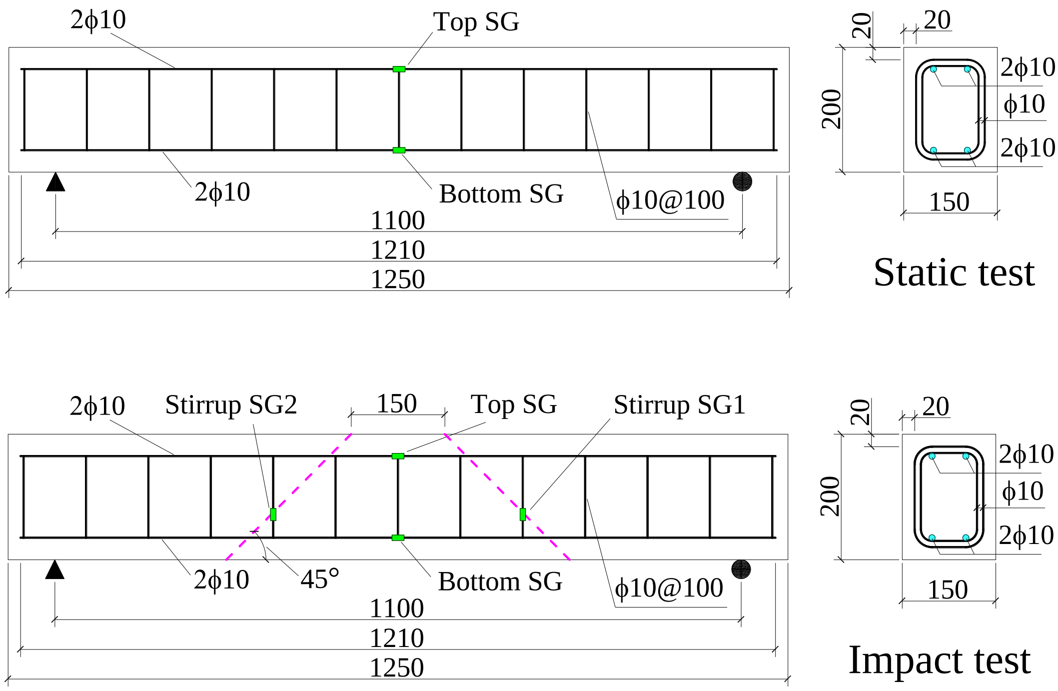

Fig. 2. Configuration of the tested beams and locations of strain gauges

Table 2 Details of the tested beams

Beam	Load condition	Compressive strength f_c' (MPa)	Tensile reinforcement ratio ρ_f (%)	Balanced reinforcement ratio ρ_{fb} (%)	Designed flexural capacity (kN)	Designed shear capacity (kN)	Strain gauges
GPC-S-39	Static	39	0.63	0.26	64.6	131.7	Top SG,

							Bottom SG
GPC-I-38	Impact	38	0.63	0.25	63.9	131.6	Top SG, Bottom SG, Stirrup SG1, Stirrup SG2
GPC-I-44	Impact	44	0.63	0.28	67.6	132.3	Top SG, Bottom SG, Stirrup SG1, Stirrup SG2

2.3. Testing program and instrumentation

2.3.1 Static test setup

The quasi-static testing setup with three-point bending configuration is shown in **Fig. 3**. The beam was simply supported with a clear span (*L*) of 1100 mm using a pin and a roller. The load was recorded by a load cell and gradually applied onto the top center of the beam using a hydraulic jack at a rate of approximately 3 mm/min. Linear variable differential transformers (LVDTs) were positioned at the midspan and *L*/4 of the beam to measure the corresponding displacements. Two strain gauges (SGs) were attached to the center of the top and bottom longitudinal bars as shown in **Fig. 2**. The main results for the static test included crack pattern, failure mode, load carrying capacity, load-deflection behaviour at midspan, and load-strain behaviour of reinforcement at midspan. The testing results were also compared with the results predicted by the existing standards such as ACI 440.1R and CSA S806.

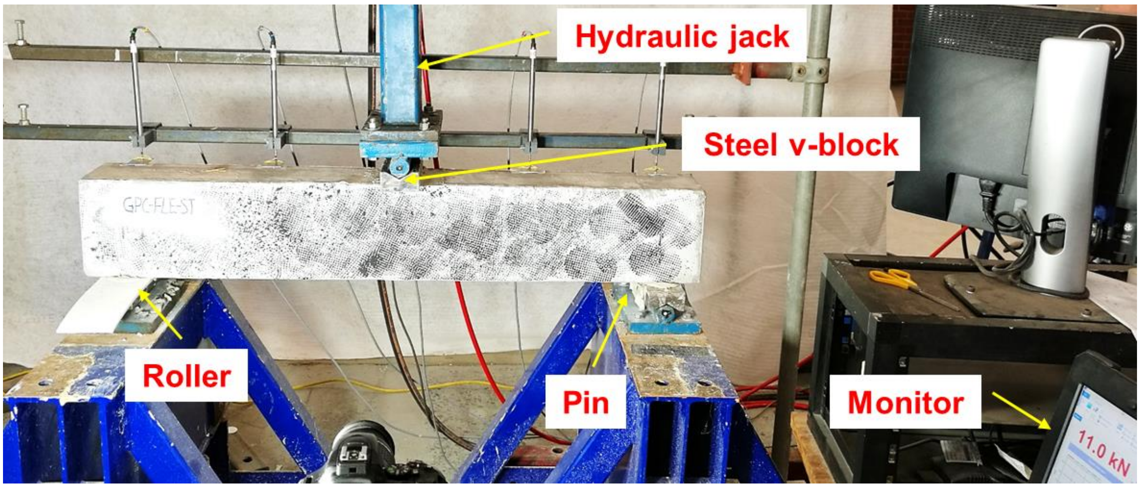

Fig. 3. Quasi-static test setup

2.3.2 Impact test setup

Two beams with slightly different GPC compressive strength (i.e. 38 MPa and 44 MPa given in **Table 2**) were tested under impact loading. The beams were simply supported on two steel plates over a pin and a steel roller, creating a clear span (L) of 1100 mm as shown in **Fig. 4**, which was the same as the static test. Two load cells were fixed onto one of the supports to measure both positive and negative reaction forces. A load cell attached to the load cell adaptor with the size of 150 mm × 200 mm × 20 mm was placed on the top surface of the beam at midspan to measure the impact force. Plaster was placed between the tested beams and the load cell adaptor to obtain an even contact surface. Four strain gauges (SGs) were installed onto the longitudinal bars and stirrups as shown in **Fig. 2**. The 203.5 kg drop hammer was released from the same height of 2 m in each test. More details about the impact test apparatus can be found in the reference [45]. A high-speed camera was used to record the failure progress and trace the impact velocity of the drop hammer and the midspan displacement of the beam at a rate of 20,000 frames per second. The impact forces and strains were recorded by the data acquisition system with the sampling rate of 50 kHz, which has been proven high enough to capture the peak impact force in the previous tests [45]. The crack pattern, failure mode, impact force, reaction force, and reinforcements strain were compared and analysed.

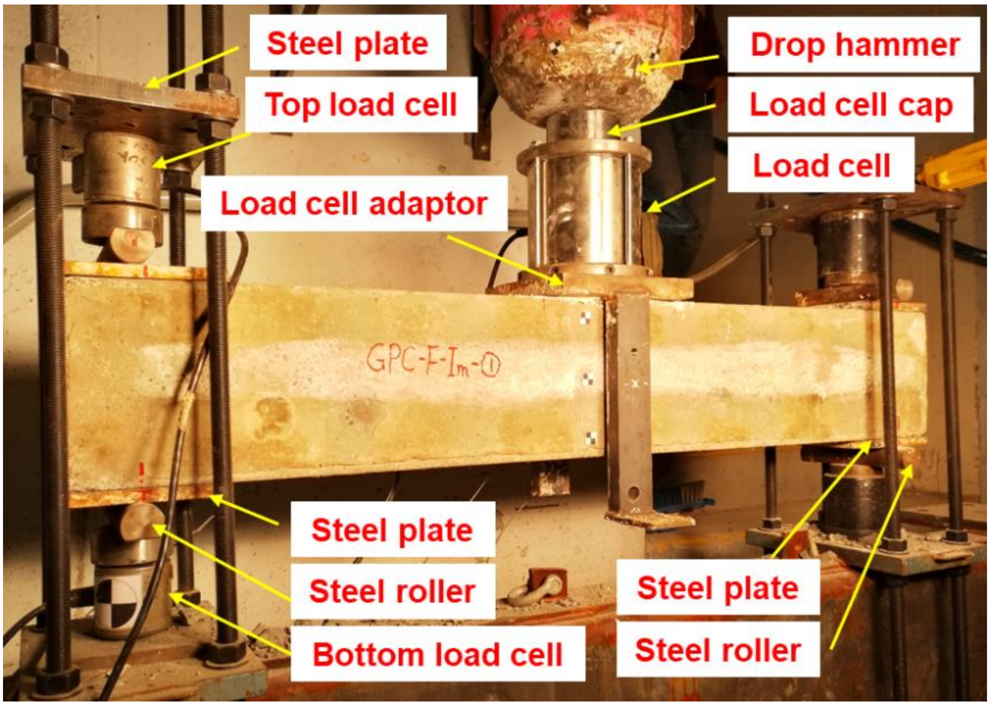

Fig. 4. Impact test setup

3. Static test results

3.1. Failure mode and crack patterns

Fig. 5 depicts the failure mode and crack pattern of Beam GPC-S-39 under static load. It primarily failed in flexure with concrete crushing on the top surface of the beam, followed by some flexure-shear cracks and shear cracks since it was over-reinforced and had relatively larger shear capacity in regard to its flexural capacity. Two main vertical cracks firstly occurred symmetrically near the midspan at a low load level (about 20 kN). When the applied load increased, the vertical cracks propagated upwards and became wider. Meanwhile, two main new vertical cracks closer to the supports appeared and gradually formed flexure-shear cracks. Further increasing the applied load, some shear cracks appeared and the two main flexural-shear cracks gradually extended to the load point. The concrete on the right side of the steel v-block then started crushing followed by the left side. At the end of loading, the beam failed with more concrete crushing and wider crack widths.

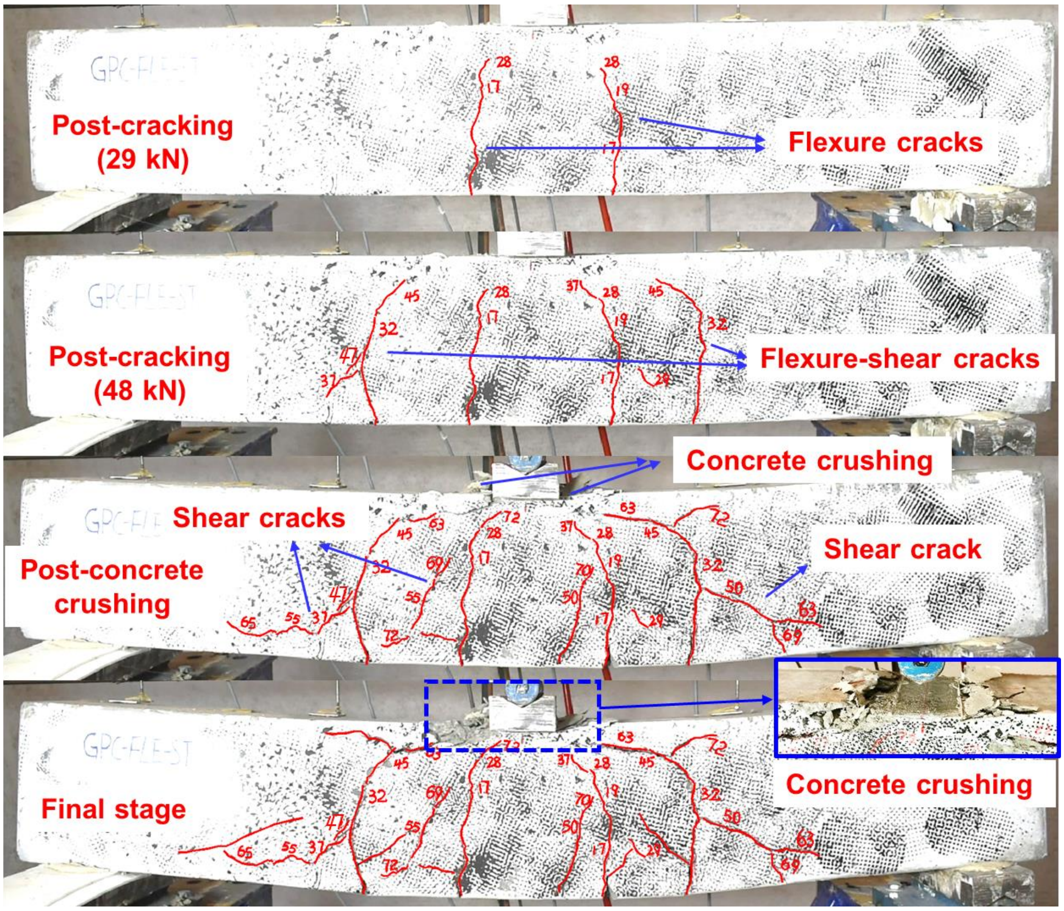

Fig. 5. Failure mode and crack propagation under quasi-static load

3.2. Quasi-static responses

Table 3 gives the quasi-static test results and **Fig. 6** shows the load-deflection curve of the applied load and the midspan deflection. It can be seen that when a new crack initiated, the load recorded by the load cell decreased slightly due to the release and redistribution of stress. The curve includes three main stages, namely, the uncracked stage (OA), the post-cracking stage (AB), and the post-concrete-crushing stage (BC), which have been also reported in the previous studies on both OPC beams [32, 33] and GPC beams [30, 34] reinforced with GFRP bars. The initial crack occurred at the load of 17.8 kN (point A) and the stiffness of the beam decreased from 59.0 kN/mm to 4.2 kN/mm. With the increasing load, the concrete crushing occurred (point B). After that, the beam was still able to carry further load up to point C.

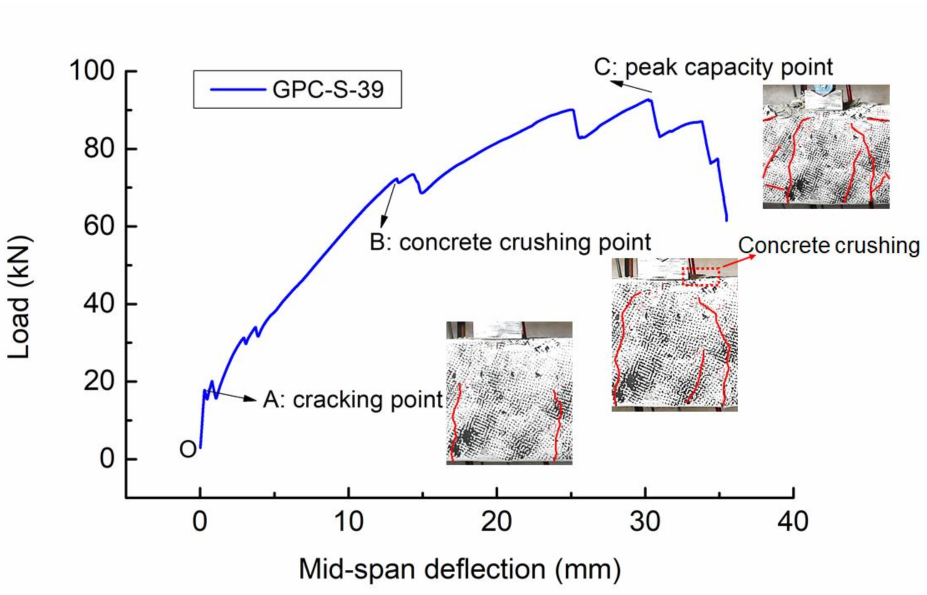

Fig. 6. Load-deflection curve of the tested beam under quasi-static load

Table 3 Quasi-static test results

Stiffness (kN/mm)			Point A (at cracking load)			Point B (at concrete crushing load)			Point C (at peak capacity load)	
OA (uncracked)	AB (post-cracking)	BC (post-concrete-crushing)	Load (kN)	Deflection (mm)	Strain of bottom bar (%)	Load (kN)	Deflection (mm)	Strain of bottom bar (%)	Load (kN)	Deflection (mm)
59.0	4.2	1.2	17.8	0.3	0.015	72.3	13.3	1.68	92.7	30.2

Fig. 7 shows the load-strain relation of the bottom longitudinal reinforcements. At the uncracked stage (OA), the reinforcement strain and stress were very small so that the load carrying capacity was mainly contributed by the GPC tensile strength. When the first crack occurred, the reinforcement strain increased sharply (AA’) to about 2,200 με since the tensile force carried by the GPC material transferred to the tensile reinforcements suddenly. The reinforcement strain then increased linearly to 16,800 με until the occurrence of concrete crushing (point B) and then the strain gauge failed.

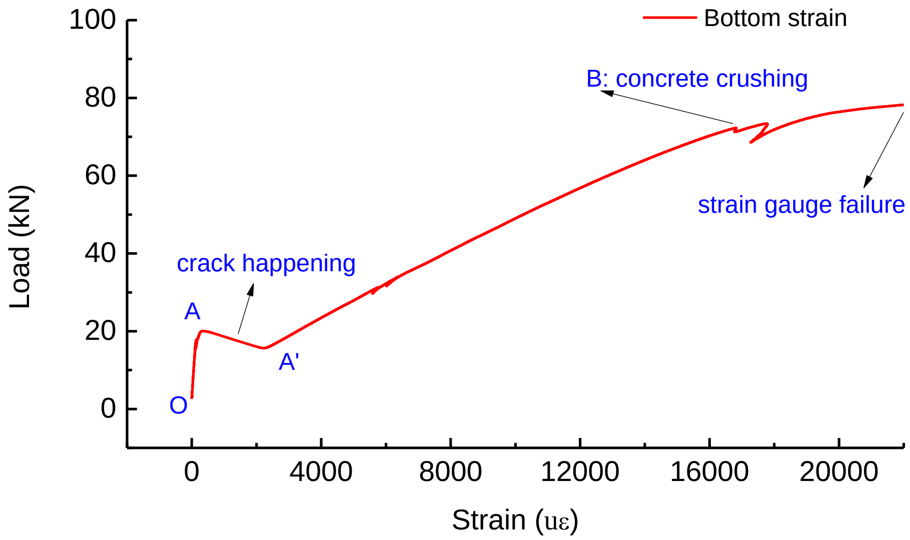

Fig. 7. Load-longitudinal strain curve of bottom reinforcements

Since there is no design Standard available for GPC beams reinforced with FRP bars, the beam load carrying capacity at the concrete crushing is predicted based on the Standards for OPC beams reinforced with FRP bars, namely, ACI 440.1R-15 [29] and CSA S806-12 [28]. **Table 4** gives the ratios of the predicted results to the test results. It is found that both ACI 440.1R-15 and CSA S806-12 can give very good prediction of the beam load carrying capacity (i.e. with the ratio of 0.89~0.99) in the present test, whereas the two codes underestimate the load-carrying capacity of the tested beams subjected to four-point bending in another study with the predicted ratios varying from 0.71 to 0.85 [30]. As reported in [30], the beams have similar concrete compressive strength and FRP bars properties as the beams in this study. The ultimate strain of concrete ε_{cu} used in the Standards (i.e. 0.003 in ACI 440.1R-15 and 0.0035 in CSA S806-12) for prediction of load carrying capacity is lower than the actual strain (0.0042-0.0048) in pure-bending zone [30], which leads to the underestimation of beam load carrying capacity. In general, the formulae from CSA S806-12 yield more accurate prediction due to the higher values of coefficient β_1 (i.e. 0.87 based on CSA S806-12 and 0.77 based on ACI 440.1R-15 in this study) and ultimate strain of concrete ε_{cu} (i.e. 0.0035 in CSA S806-12 and 0.003 in ACI 440.1R-15).

Table 4 Ratios of the predicted beam load carrying capacity to the test results

Reference	Beam	Ratios

		Type of FRP bar	Type of concrete	Concrete strength f_c' (MPa)	Reinforcement ratio ρ_f (%)	Balanced reinforcement ratio ρ_{fb} (%)	CSA [28]	ACI [29]
This study	GPC-S-39	BFRP	GPC	39	0.63	0.26	0.99	0.89
Maranan et al. [30]	SG-RGC-2-19.0	GFRP	GPC	38	1.13	0.40	0.85	0.79
	SG-RGC-3-15.9	GFRP	GPC	38	1.18	0.35	0.76	0.71
	SG-RGC-4-12.7	GFRP	GPC	38	1.00	0.30	0.80	0.74
	SG-RGC-5-15.9	GFRP	GPC	38	2.12	0.35	0.85	0.79

4. Impact test results

4.1. Failure modes and crack patterns

Two beams GPC-I-38 and GPC-I-44 showed a similar failure mode, i.e., combined flexure-shear failure with severe concrete spalling at the bottom and concrete crushing on the top of the beams as shown in **Fig. 8**. It can be found that the crack patterns of these two beams are symmetric in general. Some tie break and slight rupture occurred on the tensile BFRP bars. The two beams experienced the same failure modes with similar numbers of flexural cracks and shear cracks. Beam GPC-I-38 had severer concrete crushing on the left side, probably due to slight inclination of drop weight [46], leading to more and wider cracks on the left side than those on the right side. Compared to Beam GPC-I-38, Beam GPC-I-44 had a more symmetrical failure mode and less severe concrete crushing on the top due to the higher compressive strength. There was also one hairline vertical crack in the negative-moment area on both sides of Beam GPC-I-44, which meant the magnitude of the negative moment in Beam GPC-I-44 was a little higher than that in Beam GPC-I-38 due to the slightly higher impact force experienced by Beam GPC-I-44, which is presented and discussed later. The beams under impact load experienced much severer local damage (i.e. concrete crushing and spalling in the mid area of the bottom) and had more shear cracks distributed in a wider area along the span as compared to the beam under static load.

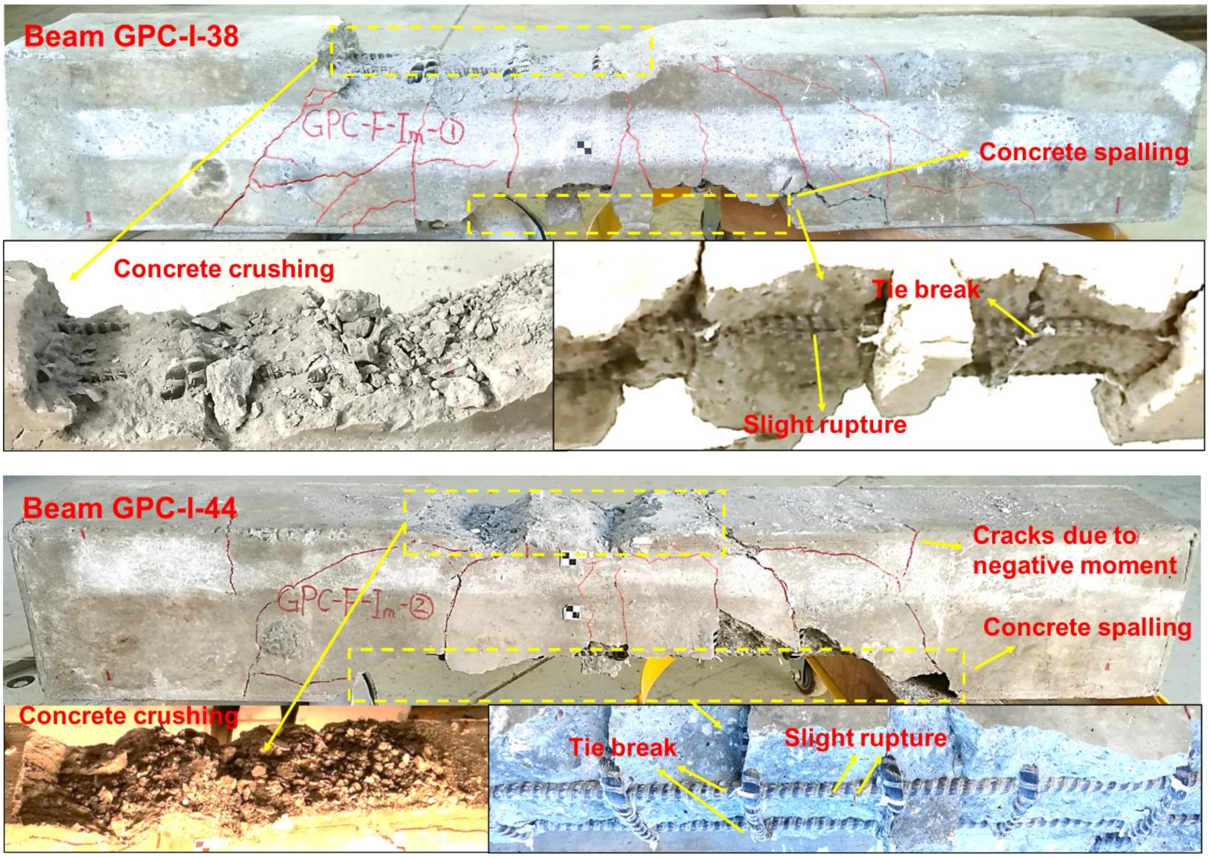

Fig. 8. Failure modes of the tested beams under impact load

Fig. 9 shows the progressive failure of the two beams captured by high-speed camera during the tests. At the instant of 1 ms, two vertical cracks and one inclined crack at an angle of about 45° were observed on the left side of Beam GPC-I-38 due to the shear failure. After the impact, the compressive waves reached the bottom of the beam and then reflected as the tensile waves, which led to tensile fracture or spalling once the tensile stress reached the dynamic tensile strength of concrete. Therefore, some longitudinal cracks were observed at the bottom of the beam at 1 ms. More vertical cracks and inclined cracks appeared on the right side of the beam from 2 ms to 5 ms. However, there was only one vertical crack on Beam GPC-I-44 at 1 ms. Then more vertical cracks, inclined cracks and longitudinal cracks gradually appeared and became wider until 5 ms. At 7 ms, no new crack appeared on both beams GPC-I-38 and GPC-I-44 and the concrete in the compressive zone beneath the load cell adaptor began to experience crushing and scabbing. Since the maximum impact forces for these two impacts were about 380 kN corresponding to a contact area of 200 mm × 150 mm, the compressive stress was about 12.7 MPa, which was less than the concrete compressive strength. The concrete crushing was therefore caused by the global bending of the beam, instead of direct impact crushing. Subsequently, the cracks further extended and the beams experienced severe crushing on the top side and spalling at the bottom side.

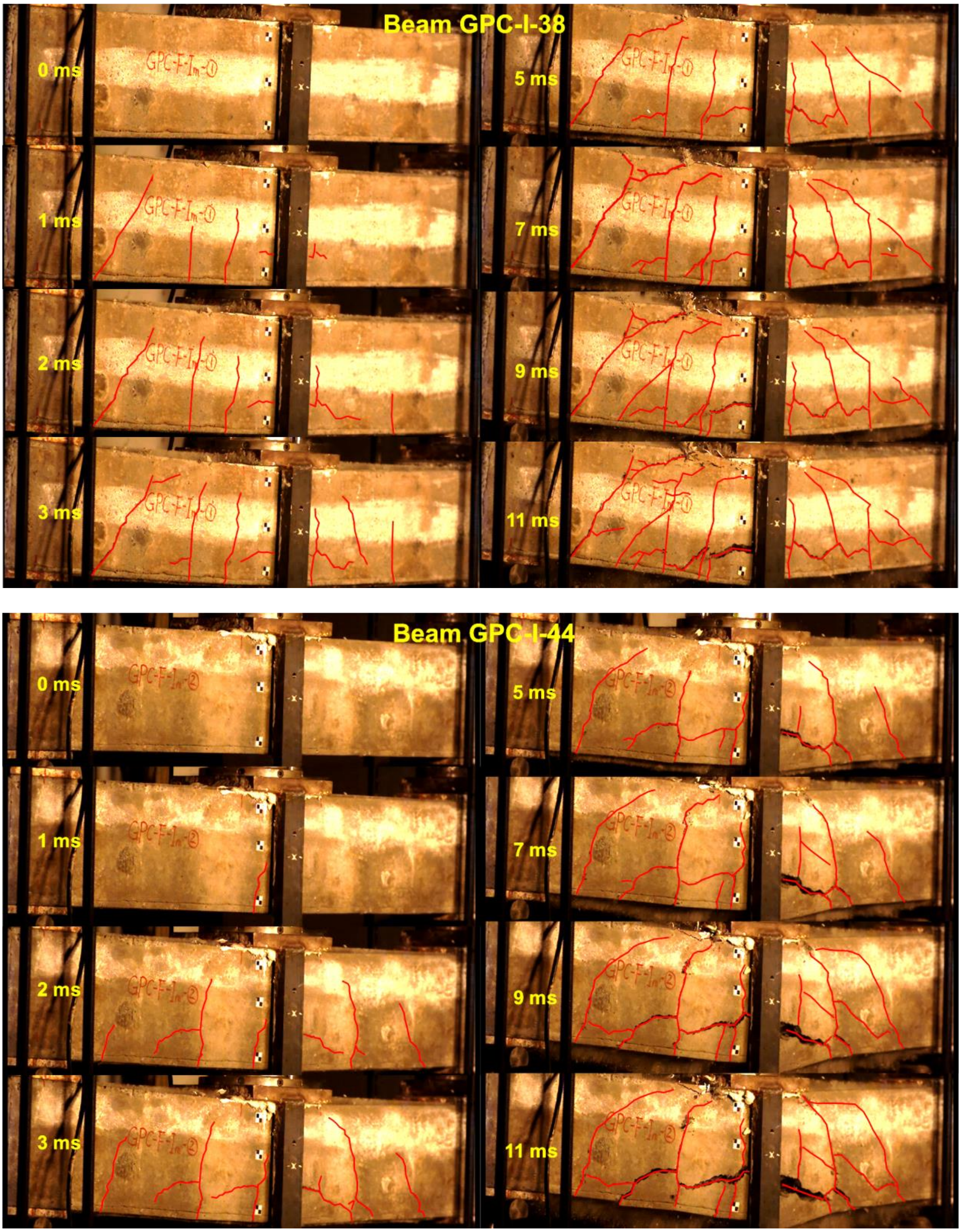

Fig. 9. Failure progress of both beams under impact load

4.2. Dynamic responses

Each beam was only subjected to one drop weight impact with the drop height of 2 m. The actual impact velocities were traced by the high-speed camera as listed in **Table 5**. **Fig. 10** shows the time histories of impact forces and reaction forces of these two beams. The impact force profile consists of a first peak with duration of about 4 ms, followed by a second peak with duration of about 2 ms. The first peak was caused by the direct drop weight impact. After the first impact, the drop hammer tended to rebound so that the impact force decreased to around zero before the second impact. The maximum impact force for Beam GPC-I-38 was 359.4 kN and 379.3 kN for Beam GPC-I-44. The slightly higher impact force on GPC-I-44 was caused by the higher contact stiffness associated with the higher concrete compressive strength of this beam. The resultant reaction force from the bottom load cell and the top load cell for beam GPC-I-38 is also shown in the figure. For Beam GPC-I-44, the reaction force was not properly recorded during the test owing to malfunction of the equipment and therefore is not presented herein.

Table 5 Impact test results

Beam	Impact velocity (m/s)	Maximum impact force (kN)	Maximum reaction force (kN)	Residual capacity (kN)	Maximum deflection (mm)	Residual deflection (mm)
GPC-I-38	5.85	359.4	117.2	-	33.2	5.3
GPC-I-44	5.69	379.3	*	89.1	28.3	5.1

Note: ‘-’: not tested; ‘*’: measurement error.

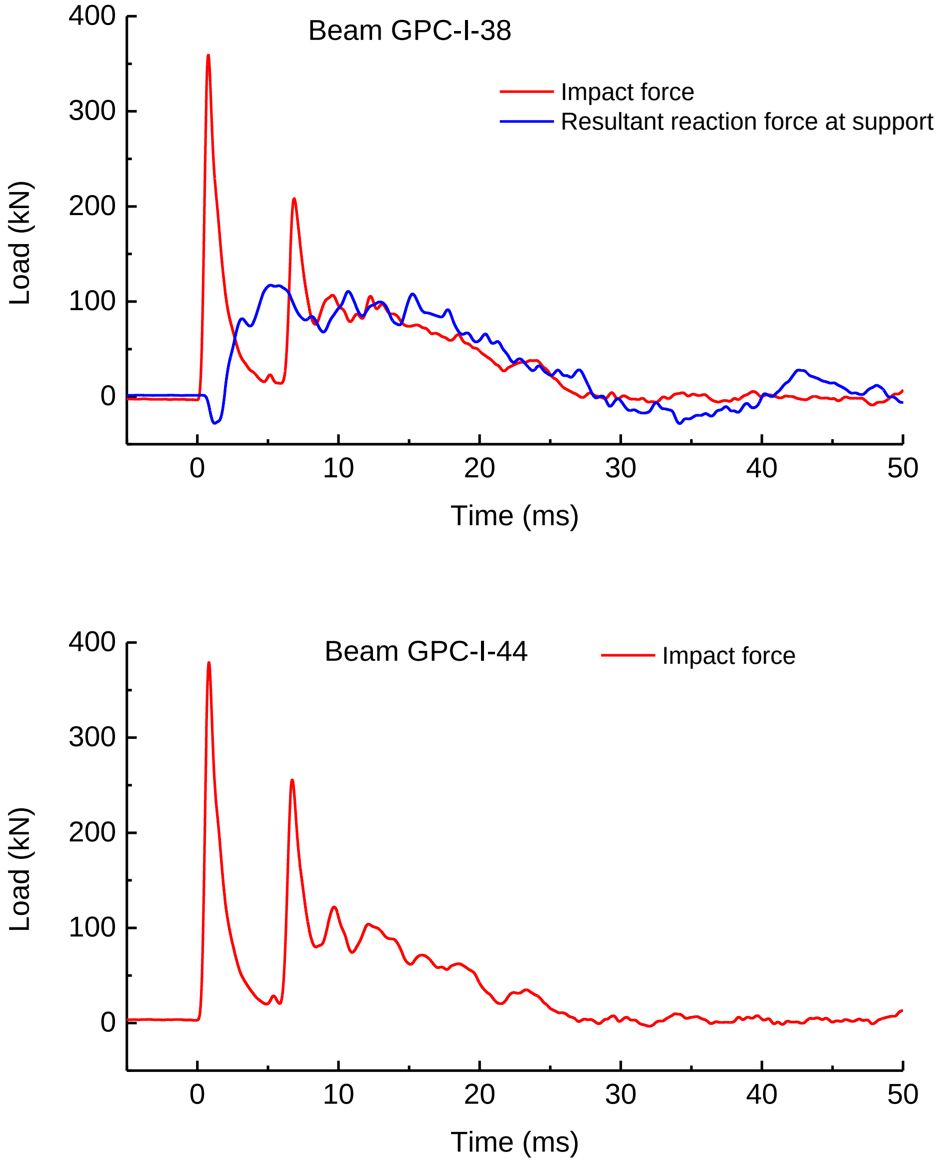

Fig. 10. Time histories of impact force and reaction force

Time delays (also called time lags) between the impact force and the reaction force were observed as shown in **Fig. 10** and detailed in **Fig. 11**. The time lags for Beam GPC-I-38 was 0.50 ms. The velocity for the stress wave propagating from the impact point at the midspan to the support was derived as 1,100 m/s. The observed time delay between the reaction force and the impact force, as well as the initial negative reaction force was associated with the impact load generated Rayleigh wave propagating from the midspan to the support as explained in [47]. During the first several milliseconds after the impact, the reaction force was not activated and then became negative because the stress wave reached the top support first, generating an uplift force before the impact force reached the peak value. During this stage, the impact force was balanced by the inertial resistance of the beam, and a large shear force was generated at the midspan of the beam. This is the reason that the beam is prone to experiencing shear-dominant failure mode under impact load [47]. When global response occurred, the reaction force became positive to balance the impact load, inertia and damping force during beam vibrations.

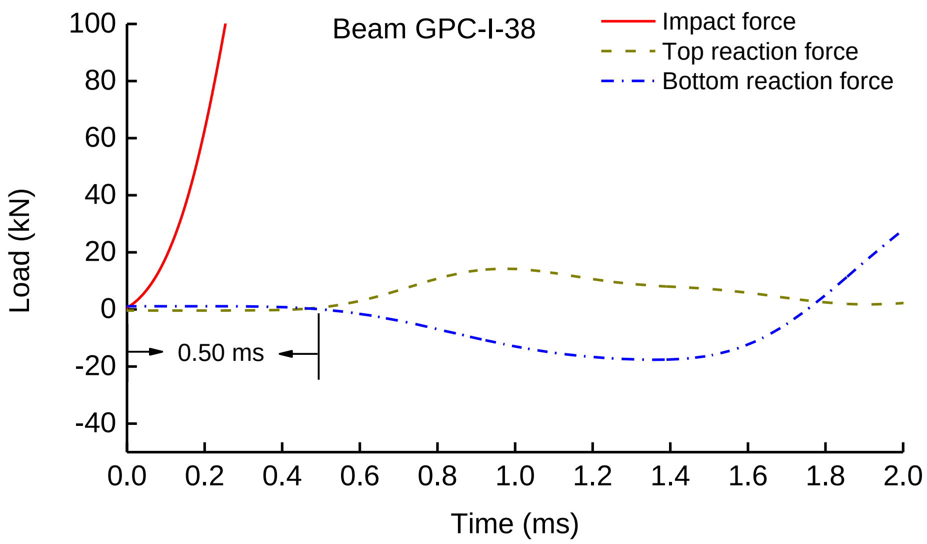

Fig. 11. Time lag of the tested Beam GPC-I-38

Fig. 12 displays the time histories of midspan deflection. The maximum deflections of the beams GPC-I-38 and GPC-I-44 were 33.2 mm and 28.3 mm, respectively, while the residual deflections were 5.3 mm and 5.1 mm, respectively. The response velocities of the midspan, namely the slopes of the curves, accelerated first upon the first impact and then slowed down to zero due to the inertial resistance force. The first impact lasted for about 7 ms, at which the displacements of the beams GPC-I-38 and GPC-I-44 were about 23 mm and 21 mm, respectively. Subsequently, the beams were subjected to a second impact. The drop hammer and the load cell moved together with the tested beams until the maximum displacement and then rebounded upwards. When the displacement decreased to the minimum at around 32 ms, the drop hammer and the load cell separated from the beam while the beam entered the phase of free vibration.

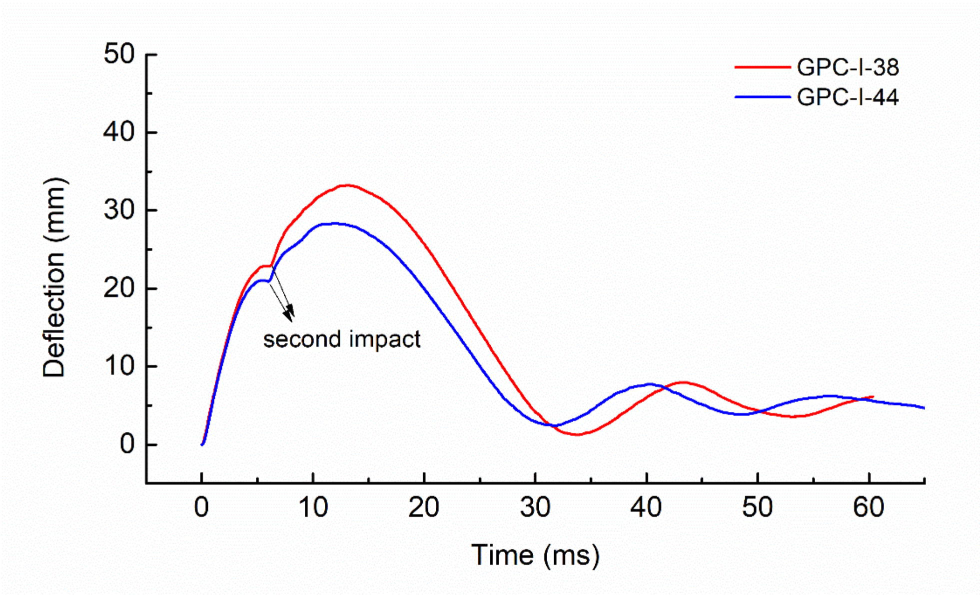

Fig. 12. Displacement time histories of the tested beams

Fig. 13 shows the reinforcement strain time histories recorded during the impact tests. Unfortunately, the bottom strain gauges of both beams were malfunctioned and not recorded in the test. The residual strain of the top longitudinal reinforcement was low, since the residual deflections of the beams were small (about 5 mm) as shown in **Fig. 12**. The strain of stirrup SG2 was higher than that of stirrup SG1 for Beam GPC-I-38, which was resulted from the severer shear damage on the left side of the beam than that on the right side as shown in **Fig. 8**. Beam GPC-I-44 had similar shear damage on both sides, and also similar peak strains in stirrups. As shown, the strain of longitudinal reinforcement was initially positive owing to change of the location of neutral axis above the top longitudinal reinforcements, negative during the global beam bending response phase, then rebounded back to positive during the free vibration phase and ended with a positive residual strain in the both beams. The positive residual strain in the top reinforcement might be attributed to the severe damage of the concrete in the midspan area as shown in **Fig. 8** and **Fig. 9**, and the membrane effect that resulted in tensile force in the reinforcement from pinned support constraints to prevent large deformation.

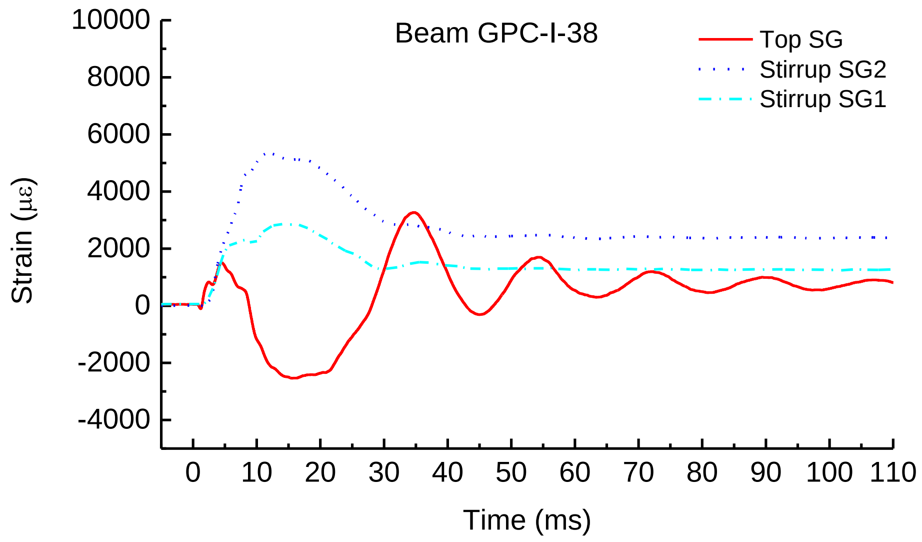

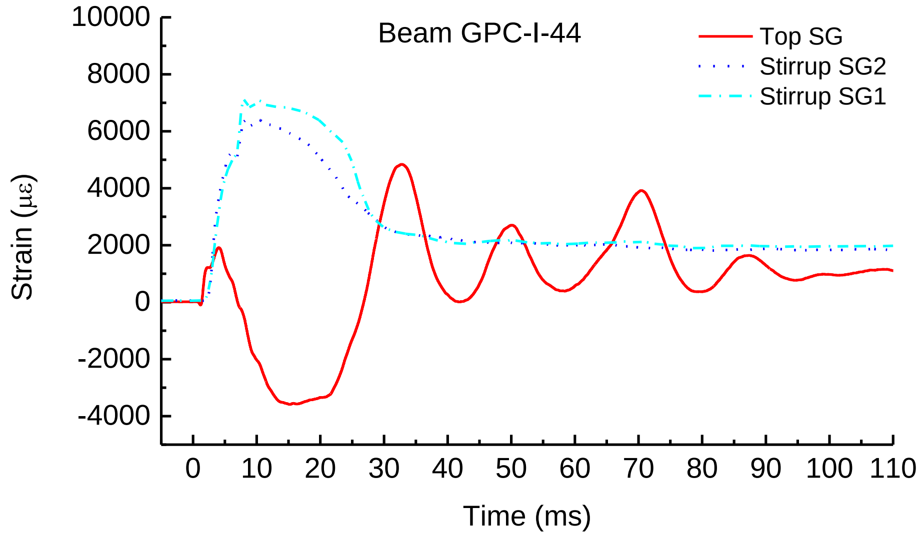

Fig. 13. Strain time histories of reinforcements

4.3. Residual capacity of the tested beams

The residual capacity of the tested beams after impact was examined in this study. **Fig. 14** shows the residual capacity test setup. Since the beams GPC-I-38 and GPC-I-44 experienced similar responses under impact, only Beam GPC-I-44 was further tested to obtain the residual capacity. **Fig. 15** shows the failure mode of Beam GPC-I-44 after the residual capacity test. Some new flexural cracks appeared near the midspan and the existing cracks became wider. The beam failed in a very brittle manner owing to the crushing failure of the stirrup-confined concrete and the rupture of the bottom BFRP bars.

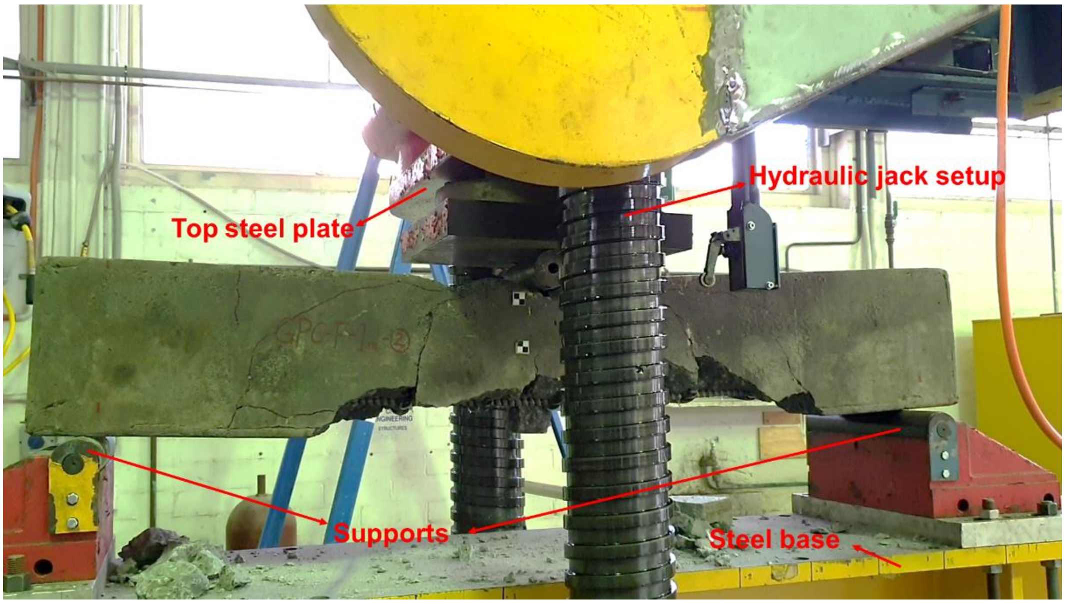

Fig. 14. Residual capacity test setup

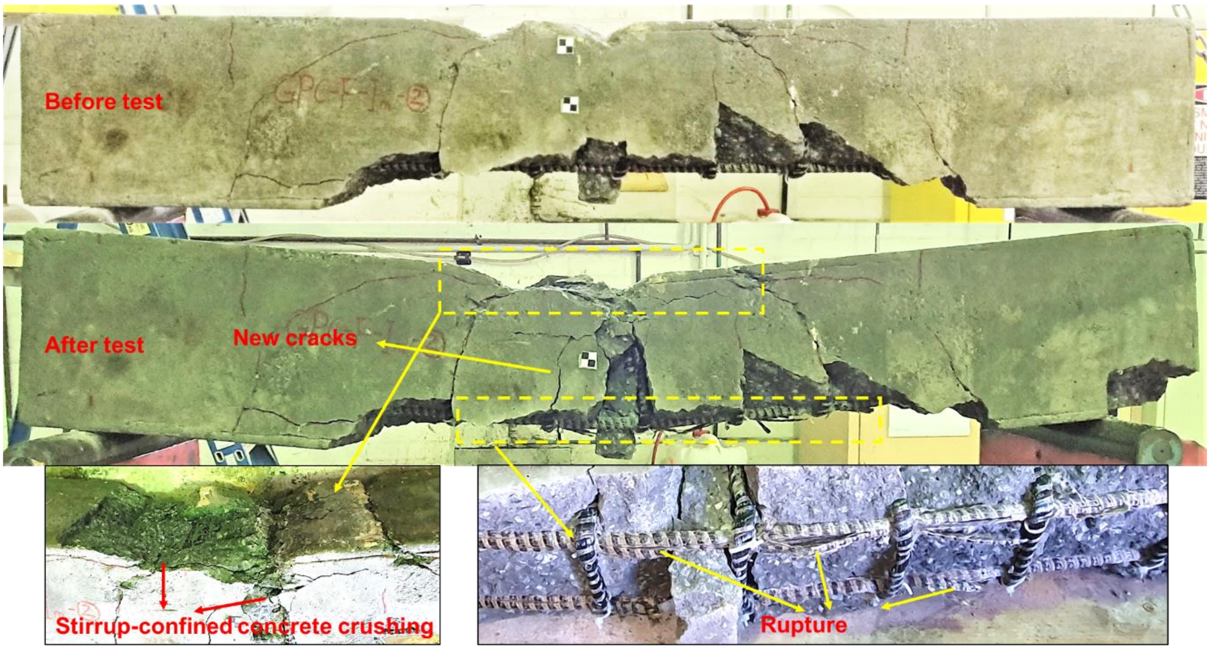

Fig. 15. Residual capacity test of Beam GPC-I-44

Fig. 16 shows the load-deflection curve of the residual capacity test of Beam GPC-I-44. The residual capacity of Beam GPC-I-44 was 89.1 kN and the corresponding deflection was 40.3 mm. The residual capacity was approximate 96% of the maximum load carrying capacity of Beam GPC-S-39 under static load because the load resistance of the beam came primarily from the reinforcement bars as GPC concrete had been severely damage, which led to a smooth load-deflection curve as compared to the one shown in **Fig. 6**.

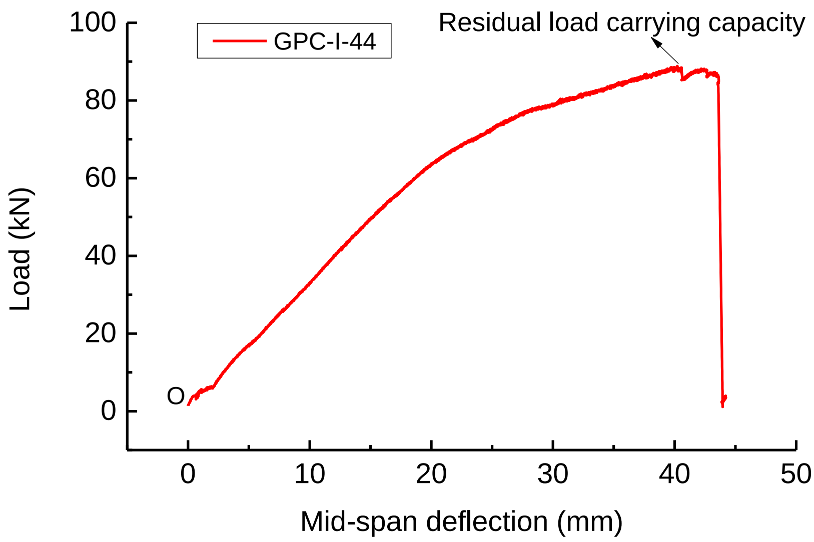

Fig. 16. Load-midspan deflection relation of Beam GPC-I-44 after impact test (residual capacity test)

5. Numerical simulations

5.1. Finite element model

The commercial software LS-DYNA [48] was used to perform the numerical simulation in this study. The numerical model was built to replicate the test, consisting of GPC beam, reinforcements, steel plates, steel rollers, drop hammer, load cell, load cell cap, as well as the load cell adaptor as shown in **Fig. 17**. Eight-node solid elements were used for GPC and other parts (i.e. drop hammer, steel plates, etc.) while Hughes-Liu beam elements with cross section integration were employed for longitudinal and stirrup bars. The steel rollers and the outside steel plates were constrained in all directions. Mesh size sensitivity was studied and the mesh sizes of 7.5 mm and 10 mm were determined for GPC beam and other parts, respectively. The keyword *Constrained_Beam_in_Solid was adopted to simulate the interaction between reinforcements and concrete. The *Automatic_Surface_to_Surface contact was used to simulate the contacts among the steel plates, steel rollers, concrete, drop hammer, load cell cap, load cell, and load cell adaptor, while the *Automatic_Surface_to_Surface_Tiebreak contact was employed to model the connection between the load cell and the load cell adaptor. The initial impact velocity of 5.8 m/s was specified for the drop hammer using the keyword *Initial_Velocity_Generation.

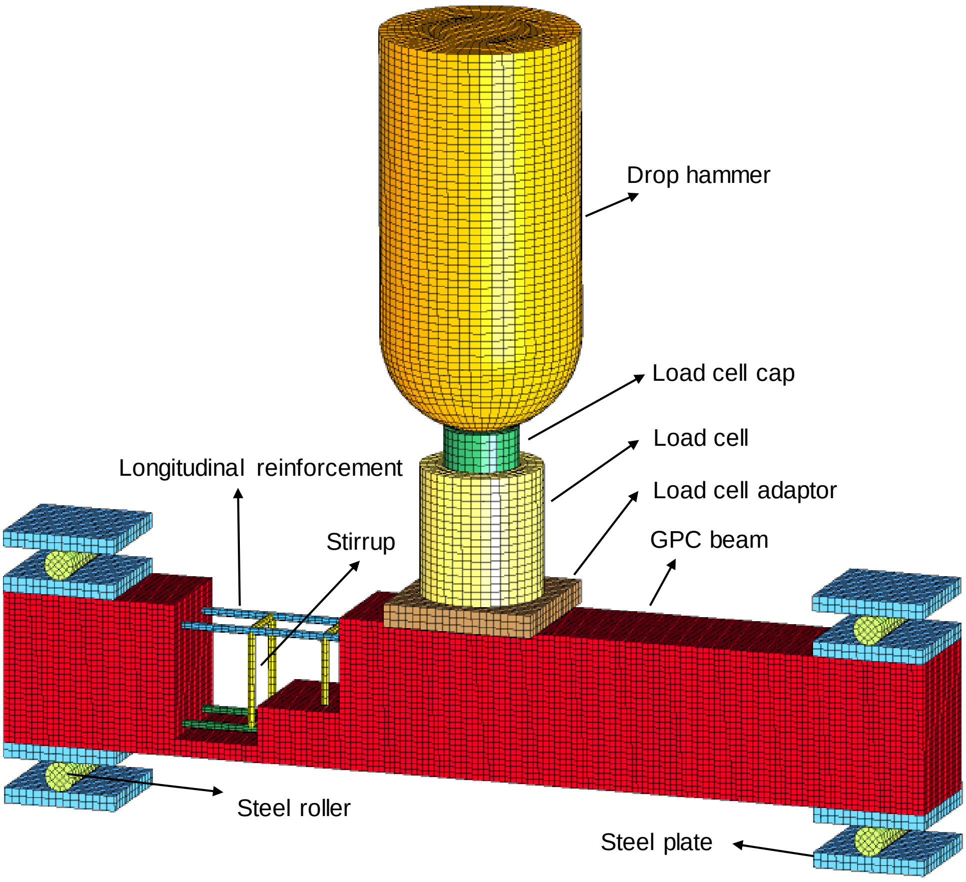

Fig. 17 Numerical model

5.2. Material models

The Karagozian & Case Concrete Model-Release III (*Mat_072R3, also called KCC model) in LS-DYNA [49] defines three failure surfaces with the consideration of effects of strain hardening, damage and strain softening [50]. It has been widely used to model the responses of concrete structures subjected to impact and blast loads, and proved yielding reliable numerical predictions [51-55]. The default parameters in *Mat_072R3 model are based on conventional OPC tests [56, 57]. However, *Mat_072R3 with specific material parameters has been used to model ultra-high performance concrete (UHPC) [57], hybrid-fibre engineered cementitious composites [58], and ultra-high performance fibre reinforced concrete (UHPFRC) [59] under impact and blast loads. In this study the KCC model was also used to model GPC material because there is no verified material model for GPC yet. To model the performance of GPC material, the default parameters in *Mat_072R3 need be modified and calibrated as GPC is more brittle than OPC [40]. The default parameters of OPC and the modified parameters of GPC in this study are listed in **Table 6**. As OPC and GPC have similar yield and peak compressive strength, most of the parameters remained as default values. Since the parameters of a_{1r} and b_1 are related to the residual strength and the damage evolution of concrete, respectively, both parameters have significant effect on concrete softening in compression. Therefore, these two parameters a_{1r} and b_1 need be modified. In addition, the damage function $\eta(\lambda)$ is a user-defined function of the effective plastic strain λ, which is relevant to the strain at peak stress and the softening of concrete. **Fig. 18** shows the modified damage function $\eta(\lambda)$ of GPC, which was based on the test results of the stress-strain relation of the GPC material.

Table 6 Parameters modified in KCC model for GPC and default parameters of OPC

Material	Density (kg/m^3)	Poisson's ratio	a_{0y}	a_{1y}	a_{2y}	a_{0m}	a_{1m}	a_{2m}	a_{1r}	a_{2r}	b_1
OPC (default)	2300	0.19	8.928E6	0.625	6.437E-9	1.182E7	0.4463	2.020E-9	0.4417	2.958E-9	1.6
GPC (modified)	2300	0.19	9.489E6	0.625	6.435E-9	1.183E7	0.4463	2.020E-9	0.3334	2.958E-9	0.6

Note: a_{0y}, a_{1y}, a_{2y}, a_{0m}, a_{1m}, a_{2m}, a_{1r}, and a_{2r} are the parameters for three failure surfaces in *Mat_072R3; b_1 is a parameter related to the compressive damage and softening behaviour of concrete.

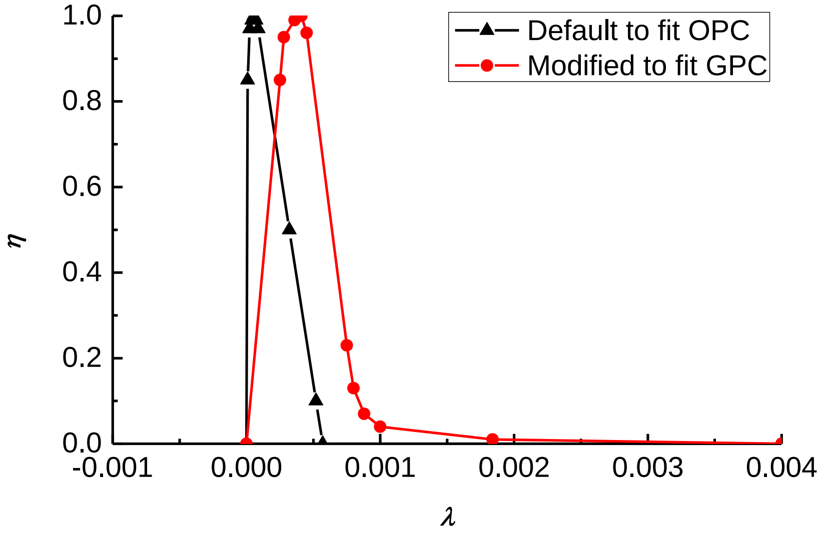

Fig. 18 Modified damage function $\eta(\lambda)$ for GPC

With the modified *Mat_072R3 for GPC material, GPC compression test with single element [58, 59] was simulated to obtain the stress-strain curve. Three cylinders from the same batch of Beam GPC-S-39 were tested as per AS 1012.9:2014 [60] and the stress-strain curves are compared with the simulation result as shown in **Fig. 19**. It can be seen that the KCC model with the modified parameters is able to represent the GPC material behaviour under compression tests.

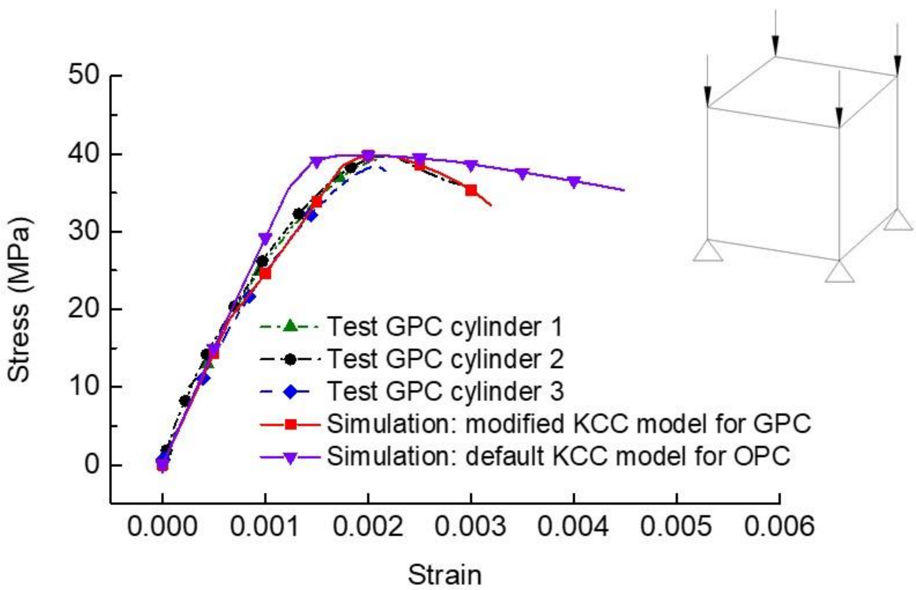

Fig. 19 Stress-strain curves of GPC material

*Mat_Piecewise_Linear_Plasticity (Mat_024) was employed to model BFRP reinforcements, steel plates, steel rollers, drop hammer, load cell cap, load cell, and load cell adaptor. Since BFRP bars have linear stress-strain curve before rupture, a very small value of 1.0E-5 [61] was adopted for the effective plastic failure strain. Load cell was simplified as a solid cylinder. Considering the configuration of internal gap inside the load cell, density of the load cell was simply determined by the equivalent mass density, i.e., the actual mass divided by the external volume of the load cell, which was 5850 kg/m^3, about 25% lower than the density of steel. For simplicity, the equivalent modulus of elasticity for the modelled load cell was also taken as 25% lower than the actual modulus of steel. The material parameters used in the numerical model are listed in **Table 7**.

Table 7 Parameters of material model

Part	Material model in LS-DYNA	Parameter	Value
GPC beam	CONCRETE_DAMAGE_REL3 (*MAT_072R3)	See **Table 6**	See **Table 6**
BFRP bars	PIECEWISE_LINEAR_PLASTICITY (*MAT_024)	Density	2000 kg/m^3
		Modulus of elasticity	55 GPa
		Poisson's ratio	0.25
		Tensile strength	1200 MPa
		Effective plastic failure strain	1.0E-5
Load cell	PIECEWISE_LINEAR_PLASTICITY (*MAT_024)	Density	5850 kg/m^3
		Modulus of elasticity	150 GPa
		Poisson's ratio	0.3
		Yield stress	500 MPa
Steel plates, steel rollers, drop hammer,	PIECEWISE_LINEAR_PLASTICITY (*MAT_024)	Density	7800 kg/m^3
		Modulus of elasticity	200 GPa

load cell cap, load cell adaptor	Poisson's ratio	0.3
	Yield stress	500 MPa

The material models of *Mat_072R3 and *Mat_024 in LS-DYNA allow users to define strength increment with strain rate by using dynamic increase factor (DIF). The DIFs for GPC [62, 63], BFRP composites [64], and steel material [65] were defined respectively to consider the strain rate effects. In order to simulate the failure mode of the beam under impact load, the erosion algorithm was applied by defining *Mat_Add_Erosion, which has been widely used in concrete structures subjected to impact and blast loads [52-54]. In this study, maximum principal strain of 0.15 for concrete, shear strain of 0.09 for top longitudinal bars, effective plastic failure strain of 1.0E-5 as listed in **Table 7** for bottom longitudinal bars, and minimum principal strain of -0.01 ('-' denotes tension) for stirrups as failure criteria were determined by trial-and-error to reach good agreement with the experimental results.

5.3. Comparison between numerical and experimental results

The concrete material model *Mat_072R3 uses effective plastic strain to characterize the concrete damage level. The crack patterns can be illustrated by the effective plastic strain contours. **Fig. 20** displays the progressive failure of the tested Beam GPC-I-44 and the corresponding effective plastic strain contours. It shows that the concrete damage predicted by numerical simulation is consistent with the crack patterns observed in the experimental test. High effective plastic strain appeared beneath the load cell adaptor at the midspan. Concrete spalling in the tension zone and concrete crushing in the compression zone were observed in both numerical and experimental results.

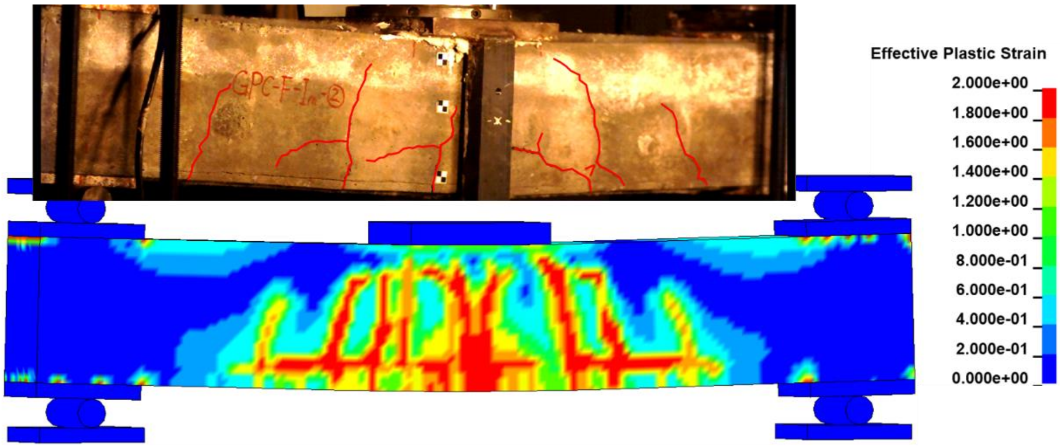
Effective Plastic Strain
2.000e+00
1.800e+00
1.600e+00
1.400e+00
1.200e+00
1.000e+00
8.000e-01
6.000e-01
4.000e-01
2.000e-01
0.000e+00

3 ms

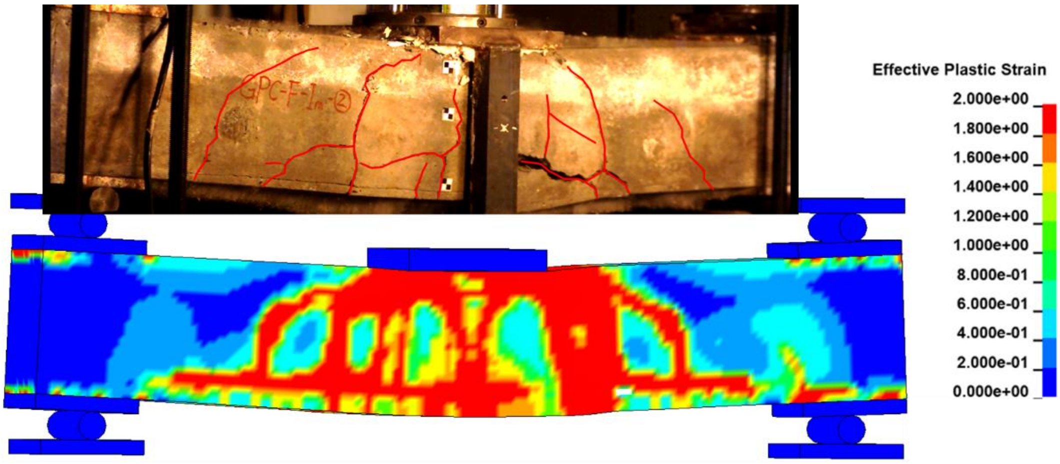
Effective Plastic Strain
2.000e+00
1.800e+00
1.600e+00
1.400e+00
1.200e+00
1.000e+00
8.000e-01
6.000e-01
4.000e-01
2.000e-01
0.000e+00

7 ms

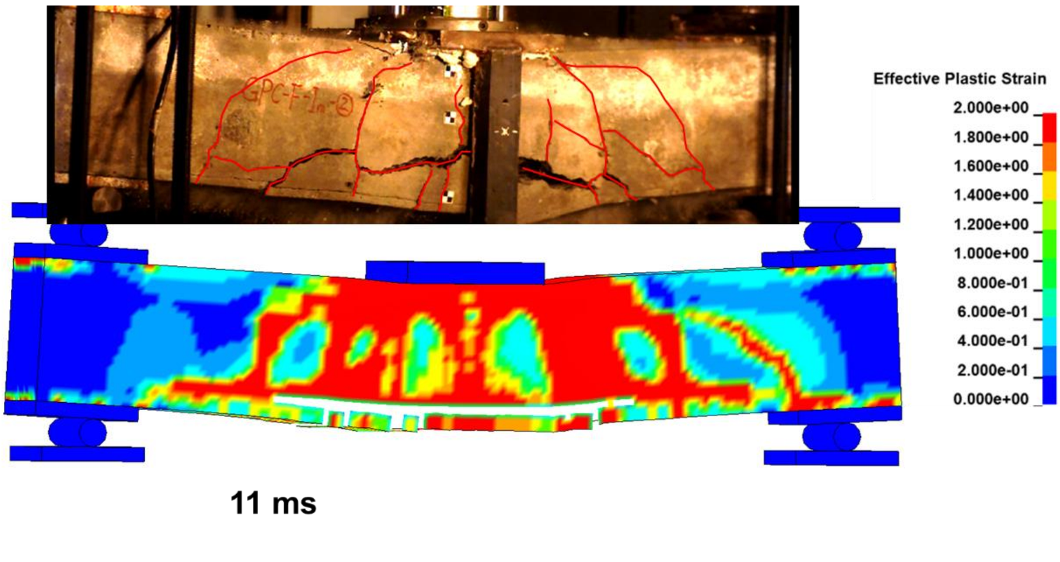
Effective Plastic Strain
2.000e+00
1.800e+00
1.600e+00
1.400e+00
1.200e+00
1.000e+00
8.000e-01
6.000e-01
4.000e-01
2.000e-01
0.000e+00

11 ms

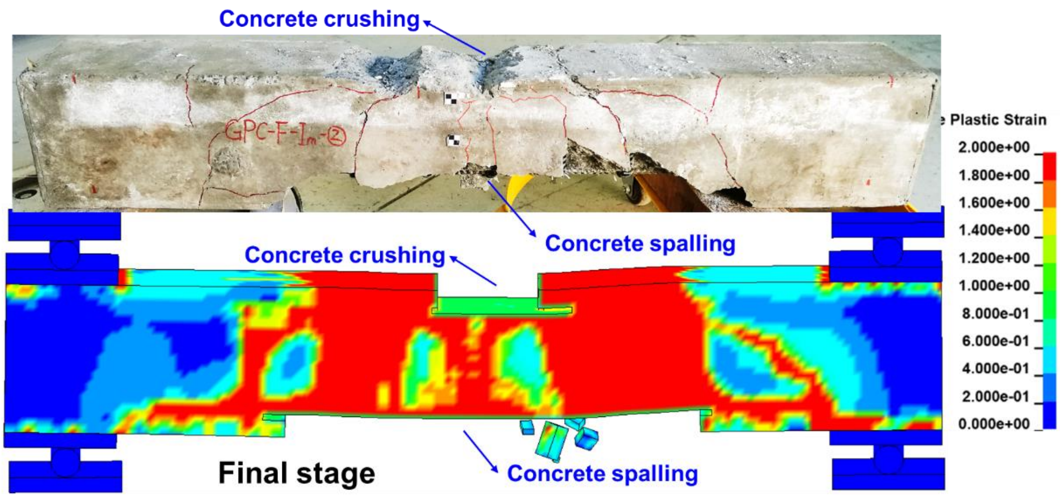

Fig. 20 Comparison of crack pattern and failure mode

Fig. 21 shows the comparison of dynamic responses between the numerical and experimental results in terms of the impact force, displacement and strain. The impact force in numerical simulation was obtained by the vertical contact force between the load cell cap and the load cell. As shown the numerical simulation well captured the impact force time history. The peak impact forces from the numerical and experimental results were 365.3 kN and 379.3 kN, respectively. The displacement response time history was also very well predicted by the numerical simulation. The maximum and residual displacements from the numerical simulation were 32 mm and 12 mm, respectively, while the corresponding values from the experimental test were 28 mm and 5 mm, respectively. Moreover, the strain time histories of top SG and stirrup SG2 predicted by numerical simulation coincided with the test results. The stirrup SG2 had the similar peak strain of 0.58% and 0.64% from the numerical and experimental results, respectively. As can be noted that the numerical simulation yielded larger displacement response, residual displacement and strain in the reinforcement bars. This could be attributed to the secondary membrane effect. In numerical simulation, the additional frictions between the rollers, steel plates and concrete due to the preload at the supports were not modelled. In experimental test, the existing frictions among these components at the supports generated some secondary tensile force along the beam axial direction to prevent large beam lateral deformations. Nonetheless, the numerical results agree reasonably well with the experimental results.

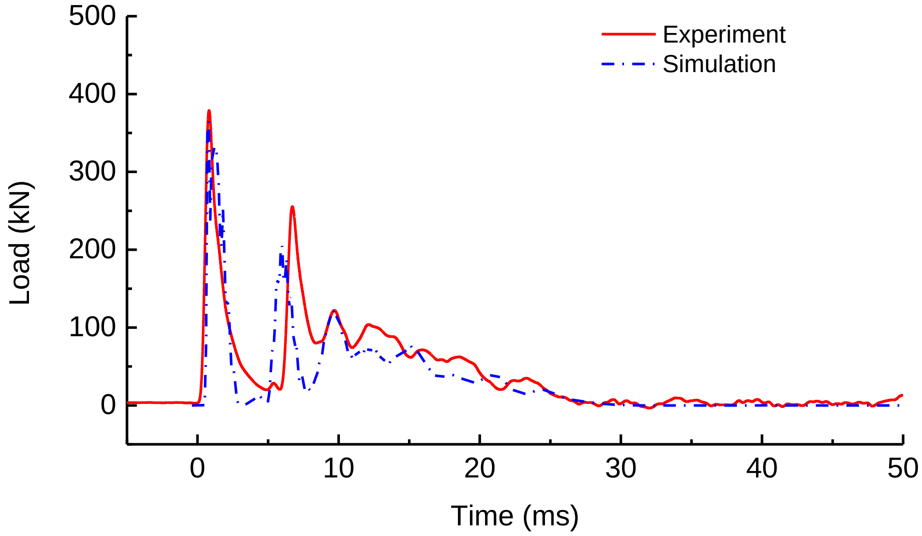
Experiment
Simulation
Load (kN)
500
400
300
200
100
0
0
10
20
30
40
50
Time (ms)

(a)

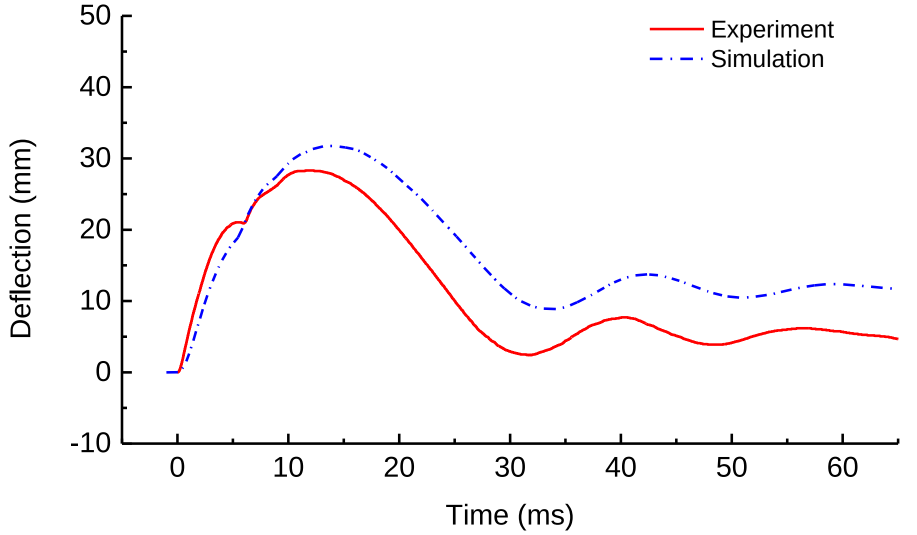
Experiment
Simulation
Deflection (mm)
50
40
30
20
10
0
-10
0
10
20
30
40
50
60
Time (ms)

(b)

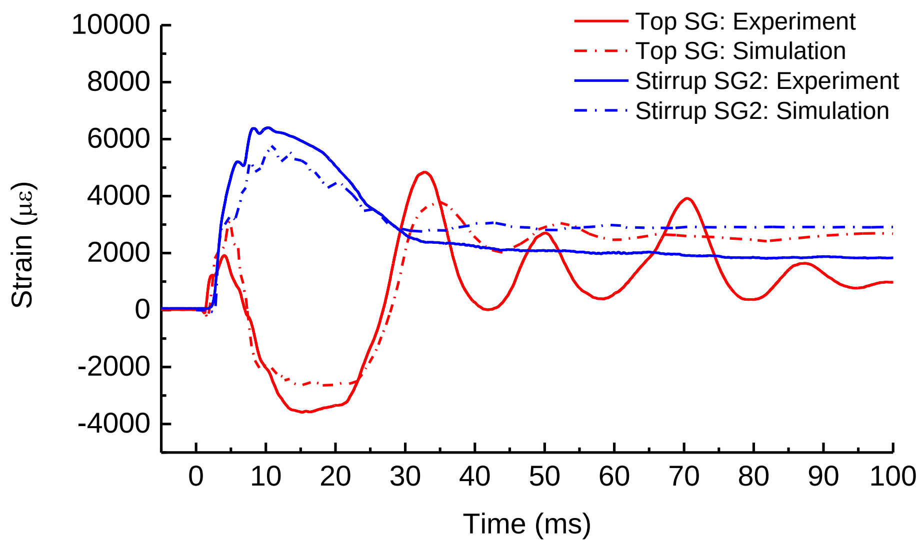

(c)

Fig. 21 Comparison of dynamic responses: (a) impact force, (b) deflection at the midspan, (c) strain of top SG and stirrup SG2

5.4. Effect of impact velocity on impact behaviour

The calibrated numerical model can be used to perform parametric simulations to investigate the influences of various loading and structural parameters on the impact responses of the GPC beams reinforced with BFRP bars. Here the effect of impact velocity on the dynamic responses of the beam was investigated. Four velocities of 3.8 m/s, 4.8 m/s, 5.8 m/s and 6.8 m/s (the corresponding drop heights: 0.7 m, 1.2 m, 1.7 m and 2.4 m) were considered. **Fig. 22** shows the failure modes and **Fig. 23** shows the midspan displacement histories of the beam. With the increasing velocities, the failure mode of the beam shifted from the flexure-governed to the punching-shear-governed along with the rupture of longitudinal BFRP bars. The width of shear cracks became wider and high effective plastic strain appeared near the 45°-inclined lines initiated from the impact point on both sides of the beam. Moreover, the maximum and residual displacements increased slightly when the impact velocity was less than 5.8 m/s while they increased sharply when the impact velocity was 6.8 m/s due to the rupture of the longitudinal BFRP bars.

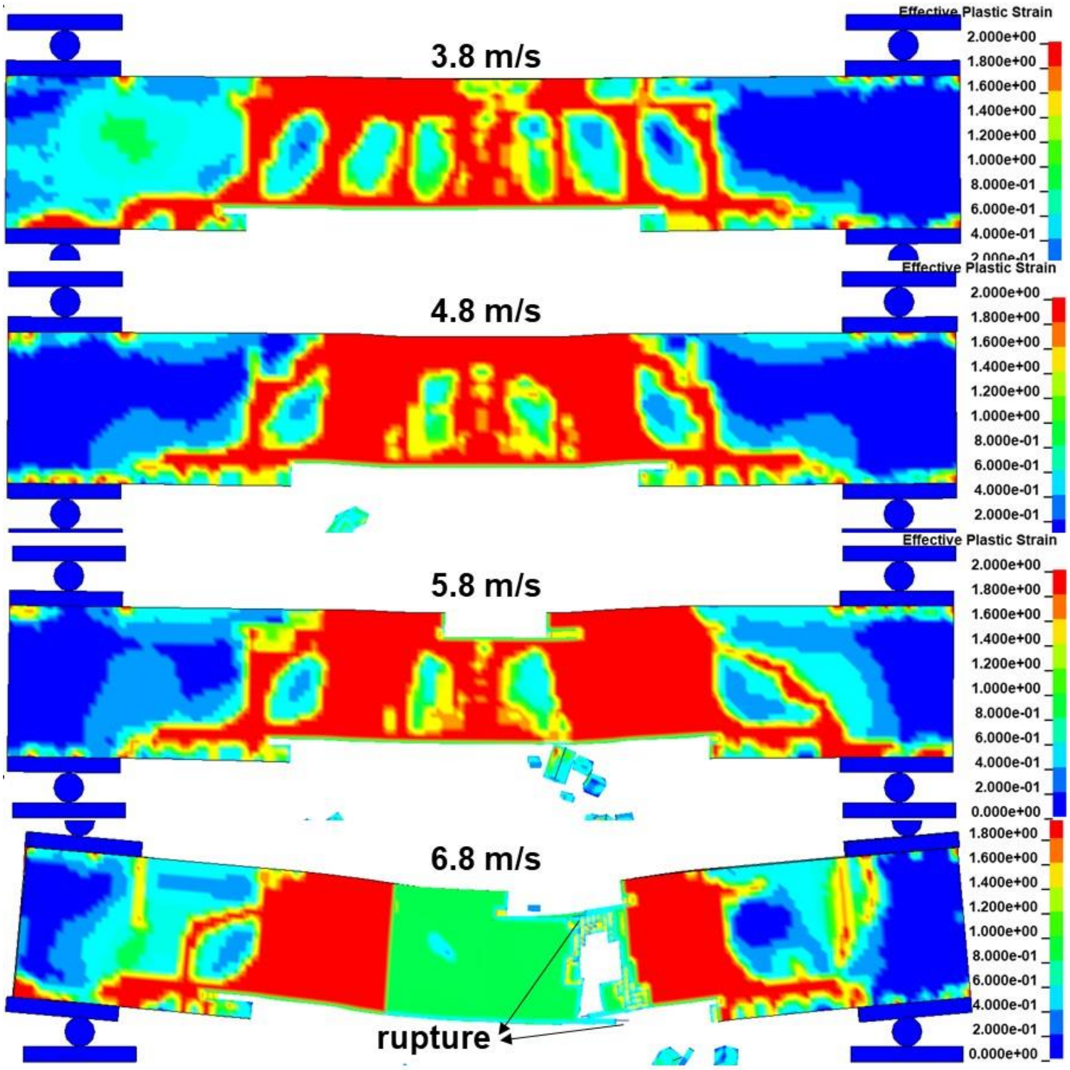

Fig. 22 Failure modes with respect to different impact velocities

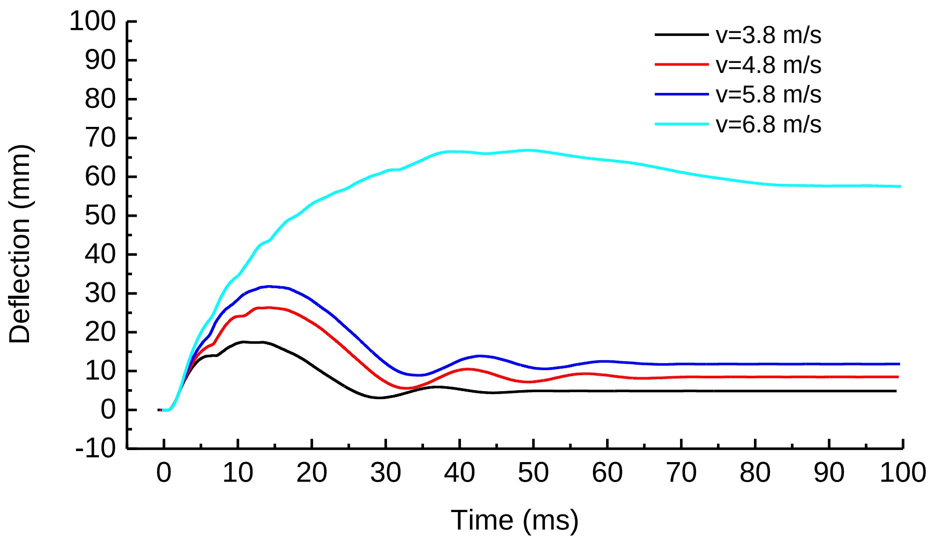

Fig. 23. Displacement time histories of the beam subjected to impact loads with different velocities

6. Conclusion

This study investigated the flexural behaviour of GPC beams reinforced with BFRP bars under static and impact loads. Based on the experimental and numerical results, the conclusions are given as follows.

1. The GPC beam reinforced with FRP bars under static load failed in flexure as expected. The load-deflection curve had three main stages, namely a steep linear segment representing the uncracked stage, a reduced slope linear segment denoting the post-cracking before concrete crushing, and a nonlinear segment representing the stage of post-concrete crushing until the complete failure of the beam.

2. The load carrying capacity of GPC beam reinforced with FRP bars under static load could be well predicted by Standards ACI 440.1R-15 and CSA S806-12. As compared to CSA S806-12 [28], the prediction based on ACI 440.1R-15 [29] was more conservative due to the smaller specified values of β_1 and ε_{cu}.

3. The GPC beam reinforced with BFRP bars failed in a flexural manner under static load, but tended to fail in the combined flexure-shear failure mode with severe local damage (i.e. concrete spalling on the bottom side and concrete crushing on the top side) under impact load.

4. The residual load carrying capacity of the damaged beam after experiencing an impact load (the drop weight of 203.3 kg at 2m height) could reach 96% of the max load carrying capacity of the beam under static load.

5. The GPC material could be simulated by using *Mat_072R3 model with the modified parameters based on the GPC material testing data. The numerical predications on the behaviours of the beam under impact load agreed well with the experimental results. With the increase of impact velocity, the predicted failure mode of the beam changed from flexure-governed to punching-shear-governed along with the rupture of longitudinal BFRP bars.

7. Acknowledgements

The authors acknowledge the financial support from the Australian Research Council (ARC) via Australian Laureate Fellowship (FL180100196). The first author also gratefully acknowledges the financial support from International Corporation and Exchange Program of Zhejiang University for PhD Student.

8. Data Availability Statement

All the result data has been reported as shown in the Figures.

9. References

[1] Huntzinger DN, Eatmon TD. A life-cycle assessment of Portland cement manufacturing: comparing the traditional process with alternative technologies. J Cleaner Prod. 2009;17:668-75.

[2] Meyer C. The greening of the concrete industry. Cem Concr Compos. 2009;31:601-5.

[3] McLellan BC, Williams RP, Lay J, Van Riessen A, Corder GD. Costs and carbon emissions for geopolymer pastes in comparison to ordinary portland cement. J Cleaner Prod. 2011;19:1080-90.

[4] Turner LK, Collins FG. Carbon dioxide equivalent (CO_2-e) emissions: A comparison between geopolymer and OPC cement concrete. Constr Build Mater. 2013;43:125-30.

[5] Gartner E. Industrially interesting approaches to “low-CO2” cements. Cem Concr Res. 2004;34:1489-98.

[6] Hardjito D, Rangan BV. Development and properties of low-calcium fly ash-based geopolymer concrete. Perth, Australia: Faculty of Engineering, Curtin University of Technology; 2005.

[7] Sarker PK, Kelly S, Yao ZT. Effect of fire exposure on cracking, spalling and residual strength of fly ash geopolymer concrete. Mater Des. 2014;63:584-92.

[8] Bakharev T. Resistance of geopolymer materials to acid attack. Cem Concr Res. 2005;35:658-70.

[9] Hardjito D, Wallah SE, Sumajouw DM, Rangan BV. On the development of fly ash-based geopolymer concrete. ACI Mater J. 2004;101:467-72.

[10] Diaz-Loya EI, Allouche EN, Vaidya S. Mechanical properties of fly-ash-based geopolymer concrete. ACI Mater J. 2011;108:300.

[11] Ryu GS, Lee YB, Koh KT, Chung YS. The mechanical properties of fly ash-based geopolymer concrete with alkaline activators. Constr Build Mater. 2013;47:409-18.

[12] Nath P, Sarker PK. Effect of GGBFS on setting, workability and early strength properties of fly ash geopolymer concrete cured in ambient condition. Constr Build Mater. 2014;66:163-71.

[13] Law DW, Adam AA, Molyneaux TK, Patnaikuni I, Wardhono A. Long term durability properties of class F fly ash geopolymer concrete. Mater Struct. 2015;48:721-31.

[14] Singh B, Ishwarya G, Gupta M, Bhattacharyya SK. Geopolymer concrete: A review of some recent developments. Constr Build Mater. 2015;85:78-90.

[15] Hassan A, Arif M, Shariq M. Use of geopolymer concrete for a cleaner and sustainable environment–A review of mechanical properties and microstructure. J Cleaner Prod. 2019.

[16] Tran TT, Pham TM, Hao H. Experimental and analytical investigation on flexural behaviour of ambient cured geopolymer concrete beams reinforced with steel fibers. Eng Struct. 2019;200:109707.

[17] Mo KH, Alengaram UJ, Jumaat MZ. Structural performance of reinforced geopolymer concrete members: A review. Constr Build Mater. 2016;120:251-64.

[18] GangaRao HV, Taly N, Vijay P. Reinforced concrete design with FRP composites. Boca Raton, Florida: CRC press, 2006.

[19] Rasheed HA, Nayal R, Melhem H. Response prediction of concrete beams reinforced with FRP bars. Compos Struct. 2004;65:193-204.

[20] Issa MS, Metwally IM, Elzeiny SM. Influence of fibers on flexural behavior and ductility of concrete beams reinforced with GFRP rebars. Eng Struct. 2011;33:1754-63.

[21] Kassem C, Farghaly AS, Benmokrane B. Evaluation of flexural behavior and serviceability performance of concrete beams reinforced with FRP bars. J Compos Constr. 2011;15:682-95.

[22] Kara IF, Ashour AF. Flexural performance of FRP reinforced concrete beams. Compos Struct. 2012;94:1616-25.

[23] Farghaly AS, Benmokrane B. Shear behavior of FRP-reinforced concrete deep beams without web reinforcement. J Compos Constr. 2013;17:04013015.

[24] Elgabbas F, Vincent P, Ahmed EA, Benmokrane B. Experimental testing of basalt-fiber-reinforced polymer bars in concrete beams. Compos Part B-Eng. 2016;91:205-18.

[25] Duic J, Kenno S, Das S. Performance of concrete beams reinforced with basalt fibre composite rebar. Constr Build Mater. 2018;176:470-81.

[26] Abdelkarim OI, Ahmed EA, Mohamed HM, Benmokrane B. Flexural strength and serviceability evaluation of concrete beams reinforced with deformed GFRP bars. Eng Struct. 2019;186:282-96.

[27] Yuan Y, Wang Z. Shear behavior of large-scale concrete beams reinforced with CFRP bars and handmade strip stirrups. Compos Struct. 2019;227:111253.

[28] CSA S806-12. Design and construction of building structures with fibre-reinforced polymers. Ontario, Canada: Canadian Standards Association; 2012.

[29] ACI 440.1R-15. Guide for the design and construction of concrete reinforced with Fiber Rienforced Polymers (FRP) bars. Farmington Hills, MI, USA: American Concrete Institute; 2015.

[30] Maranan GB, Manalo AC, Benmokrane B, Karunasena W, Mendis P. Evaluation of the flexural strength and serviceability of geopolymer concrete beams reinforced with glass-fibre-reinforced polymer (GFRP) bars. Eng Struct. 2015;101:529-41.

[31] Fan X, Zhang M. Experimental study on flexural behaviour of inorganic polymer concrete beams reinforced with basalt rebar. Compos Part B-Eng. 2016;93:174-83.

[32] Goldston MW, Remennikov A, Saleh Z, Sheikh MN. Experimental investigations on the behavior of GFRP bar reinforced HSC and UHSC beams under static and impact loading. Structures. 2019;22:109-23.

[33] Goldston M, Remennikov A, Sheikh MN. Experimental investigation of the behaviour of concrete beams reinforced with GFRP bars under static and impact loading. Eng Struct. 2016;113:220-32.

[34] Maranan G, Manalo A, Benmokrane B, Karunasena W, Mendis P, Nguyen T. Flexural behavior of geopolymer-concrete beams longitudinally reinforced with GFRP and steel hybrid reinforcements. Eng Struct. 2019;182:141-52.

[35] Ahmed HQ, Jaf DK, Yaseen SA. Flexural strength and failure of geopolymer concrete beams reinforced with carbon fibre-reinforced polymer bars. Constr Build Mater. 2020;231:117185.

[36] Banthia N, Mindess S, Bentur A, Pigeon M. Impact testing of concrete using a drop-weight impact machine. Exp Mech. 1989;29:63-9.

[37] Kishi N, Mikami H, Matsuoka K, Ando T. Impact behavior of shear-failure-type RC beams without shear rebar. Int J Impact Eng. 2002;27:955-68.

[38] Fujikake K, Li B, Soeun S. Impact response of reinforced concrete beam and its analytical evaluation. J Struct Eng. 2009;135:938-50.

[39] Pham TM, Hao H. Plastic hinges and inertia forces in RC beams under impact loads. Int J Impact Eng. 2017;103:1-11.

[40] Saleh Z, Sheikh MN, Remennikov A, Basu A. Numerical Analysis of Behavior of Glass Fiber-Reinforced Polymer Bar-Reinforced Concrete Beams under Impact Loads. ACI Struct J. 2019;116:151-60.

[41] Saleh Z, Sheikh MN, Remennikov A, Basu A. Overload Damage Mechanisms of GFRP-RC Beams Subjected to High-intensity Low-velocity Impact Loads. Compos Struct. 2019:111578.

[42] Farhan NA, Sheikh MN, Hadi MN. Investigation of engineering properties of normal and high strength fly ash based geopolymer and alkali-activated slag concrete compared to ordinary Portland cement concrete. Constr Build Mater. 2019;196:26-42.

[43] Khan MZN, Hao Y, Hao H. Synthesis of high strength ambient cured geopolymer composite by using low calcium fly ash. Constr Build Mater. 2016;125:809-20.

[44] Jiangsu Green Materials Vally New Material T&D Co. Ltd (GMV). Basalt Fiber Composite Bar. China.

[45] Pham TM, Hao H. Impact Behavior of FRP-Strengthened RC Beams without Stirrups. J Compos Constr. 2016;20.

[46] Li H, Chen W, Hao H. Influence of drop weight geometry and interlayer on impact behavior of RC beams. Int J Impact Eng. 2019;131:222-37.

[47] Pham TM, Hao H. Behavior of fiber-reinforced polymer-strengthened reinforced concrete beams under static and impact loads. International Journal of Protective Structures. 2016;8:3-24.

[48] LSTC. LS-DYNA Theory Manual. Livermore, California, USA: Livermore Software Technology Corporation; 2019.

[49] LSTC. LS-DYNA Keyword User's Munual Volume II: Material Models. Livermore, California, USA: Livermore Software Technology Corporation; 2019.

[50] Malvar LJ, Crawford JE, Wesevich JW, Simons D. A plasticity concrete material model for DYNA3D. Int J Impact Eng. 1997;19:847-73.

[51] Shi Y, Hao H, Li Z-X. Numerical derivation of pressure–impulse diagrams for prediction of RC column damage to blast loads. Int J Impact Eng. 2008;35:1213-27.

[52] Chen WS, Hao H, Chen SY. Numerical analysis of prestressed reinforced concrete beam subjected to blast loading. Mater Des. 2015;65:662-74.

[53] Li J, Hao H, Wu C. Numerical study of precast segmental column under blast loads. Eng Struct. 2017;134:125-37.

[54] Li H, Chen W, Hao H. Dynamic response of precast concrete beam with wet connection subjected to impact loads. Eng Struct. 2019;191:247-63.

[55] Do TV, Pham TM, Hao H. Impact response and capacity of precast concrete segmental versus monolithic bridge columns. J Bridge Eng. 2019;24:04019050.

[56] Zhang F, Wu C, Zhao X-L, Heidarpour A, Li Z. Experimental and numerical study of blast resistance of square CFDST columns with steel-fibre reinforced concrete. Eng Struct. 2017;149:50-63.

[57] Liu J, Wu C, Chen X. Numerical study of ultra-high performance concrete under non-deformable projectile penetration. Constr Build Mater. 2017;135:447-58.

[58] Li J, Zhang Y. Evolution and calibration of a numerical model for modelling of hybrid-fibre ECC panels under high-velocity impact. Compos Struct. 2011;93:2714-22.

[59] Mao L, Barnett S, Begg D, Schleyer G, Wight G. Numerical simulation of ultra high performance fibre reinforced concrete panel subjected to blast loading. Int J Impact Eng. 2014;64:91-100.

[60] Australia Standard. Methods of testing concrete – Method 9: Compressive strength tests -Concrete, mortar and grout specimens. Sydney, NSW, Australia: Standards Australia Limited; 2014.

[61] Almusallam TH, Elsanadedy HM, Al-Salloum YA, Alsayed SH. Experimental and numerical investigation for the flexural strengthening of RC beams using near-surface mounted steel or GFRP bars. Constr Build Mater. 2013;40:145-61.

[62] Feng KN, Ruan D, Pan Z, Collins F, Bai Y, Wang CM, et al. Effect of strain rate on splitting tensile strength of geopolymer concrete. Mag Concr Res. 2014;66:825-35.

[63] Feng KN, Ruan D, Pan Z, Collins F, Bai Y, Wang CM, et al. Mechanical behavior of geopolymer concrete subjected to high strain rate compressive loadings. Mater Struct. 2015;48:671-81.

[64] Chen W, Hao H, Jong M, Cui J, Shi Y, Chen L, et al. Quasi-static and dynamic tensile properties of basalt fibre reinforced polymer. Compos Part B-Eng. 2017;125:123-33.

[65] Malvar LJ. Review of static and dynamic properties of steel reinforcing bars. ACI Mater J. 1998;95:609-16.